UNIVERSIDADE FEDERAL DO PARANÁ

IRINA ISABEL SALAZAR ARGOTI

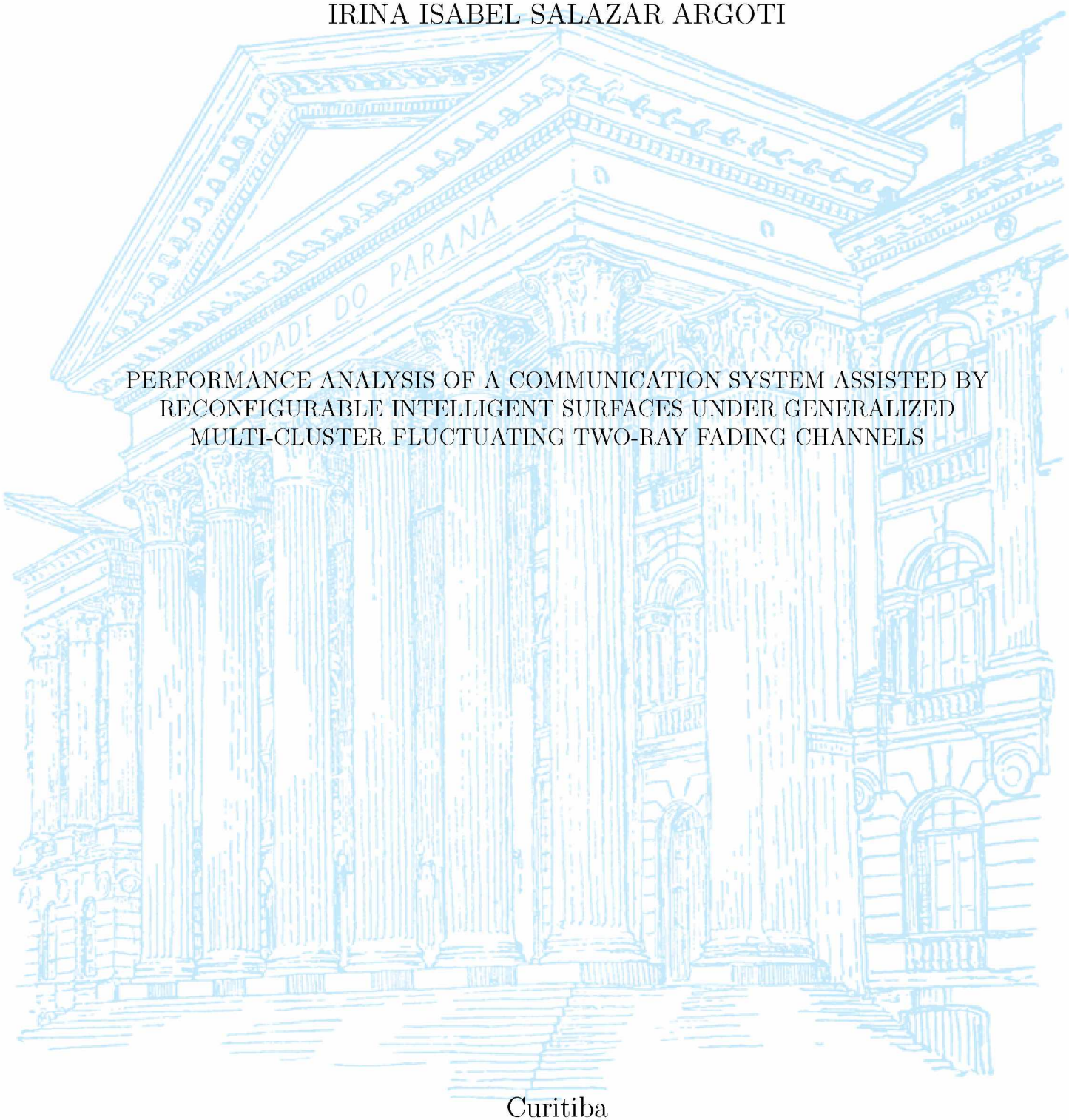

PERFORMANCE ANALYSIS OF A COMMUNICATION SYSTEM ASSISTED BY RECONFIGURABLE INTELLIGENT SURFACES UNDER GENERALIZED MULTI-CLUSTER FLUCTUATING TWO-RAY FADING CHANNELS

Curitiba
2025

IRINA ISABEL SALAZAR ARGOTI

PERFORMANCE ANALYSIS OF A COMMUNICATION SYSTEM ASSISTED BY RECONFIGURABLE INTELLIGENT SURFACES UNDER GENERALIZED MULTI-CLUSTER FLUCTUATING TWO-RAY FADING CHANNELS

Dissertação apresentada ao curso de Pós-Graduação em Engenharia elétrica, Setor de Tecnologia, Universidade Federal do Paraná, como requisito parcial à obtenção do título de Mestre em Engenharia Elétrica.

Orientador: Prof. Dr. Evelio Martín G. Fernández
Co Orientador: Prof. Dr. Henry Ramiro Carvajal Mora

Curitiba
2025

DADOS INTERNACIONAIS DE CATALOGAÇÃO NA PUBLICAÇÃO (CIP)
UNIVERSIDADE FEDERAL DO PARANÁ
SISTEMA DE BIBLIOTECAS – BIBLIOTECA DE CIÊNCIA E TECNOLOGIA

Argoti, Irina Isabel Salazar
Performance analysis of a communication system assisted by reconfigurable intelligent surfaces under generalized multi-cluster fluctuating two-ray fading channels / Irina Isabel Salazar Argoti. – Curitiba, 2025.
1 recurso on-line : PDF.

Dissertação (Mestrado) - Universidade Federal do Paraná, Setor de Tecnologia, Programa de Pós-Graduação em Engenharia Elétrica.

Orientador: Evelio Martín García Fernández
Coorientador: Henry Ramiro Carvajal Mora

1. Sistema de comunicação. 2. Distribuição (Teoria da probabilidade). 3. Canais de desvanecimento. 4. Superfícies inteligentes reconfiguráveis. I. Universidade Federal do Paraná. II. Programa de Pós-Graduação em Engenharia Elétrica. III. García Fernández, Evelio Martín. IV. Carvajal Mora, Henry Ramiro. V. Título.

Bibliotecário: Elias Barbosa da Silva CRB-9/1894

MINISTÉRIO DA EDUCAÇÃO
SETOR DE TECNOLOGIA
UNIVERSIDADE FEDERAL DO PARANÁ
PRÓ-REITORIA DE PÓS-GRADUAÇÃO
PROGRAMA DE PÓS-GRADUAÇÃO ENGENHARIA ELÉTRICA - 40001016043P4

TERMO DE APROVAÇÃO

Os membros da Banca Examinadora designada pelo Colegiado do Programa de Pós-Graduação ENGENHARIA ELÉTRICA da Universidade Federal do Paraná foram convocados para realizar a arguição da dissertação de Mestrado de **IRINA ISABEL SALAZAR ARGOTI**, intitulada: **Performance Analysis of a Communication System Assisted by Reconfigurable Intelligent Surfaces under Generalized Multi-Cluster Fluctuating Two-Ray Fading Channels**, sob orientação do Prof. Dr. EVELIO MARTÍN GARCÍA FERNÁNDEZ, que após terem inquirido a aluna e realizada a avaliação do trabalho, são de parecer pela sua APROVAÇÃO no rito de defesa.

A outorga do título de mestra está sujeita à homologação pelo colegiado, ao atendimento de todas as indicações e correções solicitadas pela banca e ao pleno atendimento das demandas regimentais do Programa de Pós-Graduação.

Curitiba, 18 de Dezembro de 2025.

Assinatura Eletrônica
19/12/2025 11:25:28.0
EVELIO MARTÍN GARCÍA FERNÁNDEZ
Presidente da Banca Examinadora

Assinatura Eletrônica
19/12/2025 13:44:08.0
LUIS HENRIQUE ASSUMPÇÃO LOLIS
Avaliador Interno (UNIVERSIDADE FEDERAL DO PARANÁ)

Assinatura Eletrônica
20/12/2025 16:23:05.0
NATHALY VERÓNICA OROZCO GARZÓN
Avaliador Externo (UNIVERSIDAD DE LAS AMéRICAS)

"To my siblings and my Chloe, for their complicity, laughter, and unconditional love.
To my mom Vivi, my blessing and steadiness through uncertainty
To my family, whose support shaped every step of this journey.
To Fernando, my constant and partner in crime.
And to myself, for not giving up."

ACKNOWLEDGMENTS

I would like to express my deepest gratitude to my professors, Dr. Evelio Martín G. Fernández and Dr. Henry Ramiro Carvajal, whose guidance, knowledge, and constant support were fundamental throughout the development of this work. Their commitment to excellence has shaped not only this thesis, but also my growth as a researcher and engineer.

I sincerely thank to Coordenação de Aperfeiçoamento de Pessoal de Nível Superior (CAPES) for the opportunity to study in Brazil, for supporting my academic development, and for granting me the possibility to grow as a researcher. This experience expanded my scientific and professional horizons in meaningful ways.

To my siblings, Alejo, Ariel, Isaac and my little Chloe, thank you for being my daily strength, my joy, and my emotional anchor. To my parents and grandparents, I am grateful for your unconditional love and for accompanying me every step of this journey.

My heartfelt appreciation goes to my mom Vivi, my greatest blessing. Her unwavering support, wisdom, and presence have been my safe place, especially during moments of uncertainty.

To my love, Fernando, thank you for believing in me wholeheartedly, for reminding me of my worth, and for being a source of peace and encouragement.

Finally, to my dear friends Santy and Jessy, thank you for staying, for your patience, and for never giving up on our friendship.

RESUMO

As Superfícies Inteligentes Reconfiguráveis (RIS) destacam-se como uma tecnologia promissora para ampliar a cobertura e a confiabilidade em redes sem fio de próxima geração. Contudo, o desempenho de sistemas assistidos por RIS sob desvanecimento realista em altas frequências ainda é pouco explorado. Esta dissertação apresenta o primeiro estudo analítico de desempenho de sistemas assistidos por RIS operando sob o modelo Multi-Cluster Fluctuating Two-Ray (MFTR), o qual é particularmente adequado para cenários mmWave por modelar múltiplos clusters de espalhamento e flutuações nos componentes especulares. Expressões aproximadas em forma fechada para a probabilidade de falha (*outage probability*) e para a probabilidade média de erro de bit (ABEP), sob modulação M-QAM, são derivadas e validadas por simulações de Monte Carlo. Os resultados mostram que o aumento do número de elementos da RIS gera ganhos expressivos no orçamento de enlace; por exemplo, ao aumentar N de 50 para 200, observa-se uma redução de aproximadamente 13 dB na potência de transmissão necessária para atingir uma ABEP de 10^{-3}. Além disso, simulações indicam que a incorporação da técnica Signal Space Diversity (SSD) melhora o desempenho do sistema, especialmente quando o número de elementos da RIS é reduzido, aumentando a diversidade sem exigir hardware adicional. De forma geral, os resultados confirmam que a combinação de RIS, MFTR e SSD é uma abordagem eficaz para aumentar a confiabilidade de sistemas sem fio em ambientes de propagação severos.

Palavras-chave: *Superfícies Inteligentes Reconfiguráveis, desvanecimento MFTR, desvanecimento FTR, modelos de desvanecimento generalizados, probabilidade de queda, probabilidade média de erro de bit, SSD, 5G/6G.*

ABSTRACT

Reconfigurable Intelligent Surfaces (RIS) have emerged as a promising technology to enhance coverage and reliability in next-generation wireless networks. However, the performance of RIS-assisted systems under realistic high-frequency fading conditions remains insufficiently explored. This dissertation presents the first analytical performance study of RIS-assisted systems operating under the Multi-Cluster Fluctuating Two-Ray (MFTR) fading model, which is particularly suitable for mmWave scenarios as it captures multiple scattering clusters and fluctuations of specular components. Closed-form approximate expressions for the outage probability and the average bit error probability (ABEP), under M-QAM modulation, are derived and validated through Monte Carlo simulations. The results show that increasing the number of RIS elements leads to significant link-budget gains; for instance, increasing N from 50 to 200 yields an approximate 13 dB reduction in the required transmit power to achieve an ABEP of 10^{-3}. In addition, simulation results indicate that incorporating Signal Space Diversity (SSD) further improves system performance, particularly when the number of RIS elements is limited, by enhancing diversity without requiring additional hardware. Overall, the results confirm that the combination of RIS, MFTR, and SSD is an effective approach to improve the reliability of wireless communication systems operating in severe propagation environments.

Keywords: *Reconfigurable Intelligent Surfaces, MFTR fading, FTR fading, generalized fading models, outage probability, average bit error probability, SSD, 5G/6G.*

LIST OF FIGURES

LIST OF TABLES

LISTA DE SIGLAS

ABEP	Average Bit Error Probability
AWGN	Additive White Gaussian Noise
BER	Bit Error Rate
CDF	Cumulative Distribution Function
CSI	Channel State Information
FTR	Fluctuating Two-Ray
IFTR	Inverse Fluctuating Two-Ray
IoT	Internet of Things
LoS	Line-of-Sight
MFTR	Multi-Cluster Fluctuating Two-Ray
MGF	Moment Generating Function
MIMO	Multiple-Input Multiple-Output
mmWave	Millimeter Wave
NLoS	Non-Line-of-Sight
OP	Outage Probability
PDF	Probability Density Function
QAM	Quadrature Amplitude Modulation
RIS	Reconfigurable Intelligent Surface
SNR	Signal-to-Noise Ratio
SSD	Signal Space Diversity
sub-THz	Sub-Terahertz
THz	Terahertz
Tx	Transmitter
Rx	Receiver
URLLC	Ultra-Reliable Low-Latency Communications

LISTA DE SÍMBOLOS

P_t	Transmit power (in watts or dBm)
P_r	Received power
d_1, d_2	Distances of the Tx–RIS and RIS–Rx links
α_1, α_2	Path-loss exponents of the Tx–RIS and RIS–Rx links
K_1, K_2	Path-loss intercepts (propagation constants)
N	Number of reflecting elements in the RIS
h_n, g_n	Complex fading coefficients of the RIS–Rx and Tx–RIS links
$\Theta =$	RIS phase-shift matrix
$\text{diag}(e^{j\theta_1}, \ldots, e^{j\theta_N})$	
γ	Instantaneous signal-to-noise ratio (SNR)
γ_{th}	SNR threshold for outage probability
$\bar{\gamma}$	Average SNR
$p_\gamma(\gamma)$	Probability density function of SNR
P_{out}	Outage probability
P_b or P_e	Average bit error probability
C_{erg}	Ergodic channel capacity
m	Shadowing (fluctuation) parameter in MFTR model
K	Specular-to-diffuse average power ratio
Δ	Relative similarity between specular components ($0 \leq \Delta \leq 1$)
μ	Number of multipath clusters
ω_i,λ_i,v_i	MFTR mixture weights, shape, and scale parameters
Φ	RIS phase configuration matrix
W	SSD rotation matrix
λ	Design parameter of SSD rotation
s,r	Non-rotated and rotated transmitted symbol vectors
n	Additive white Gaussian noise sample

σ_n^2	Noise power
Ψ	Instantaneous received SNR after RIS combining
η_r,σ_r^2	Mean and variance of the equivalent cascaded channel
R_{th}	Target transmission rate (bits/s/Hz)
B	Channel bandwidth
Ω	Average received power in fading model
$I_\nu(\cdot)$	Modified Bessel function of the first kind
$\Gamma(\cdot)$	Gamma function
$\gamma(a,x)$	Lower incomplete gamma function
${}_2F_1(\cdot)$	Gauss hypergeometric function

TABLE OF CONTENTS

1 INTRODUCTION

1.1 Background and Motivation

The evolution toward fifth-generation (5G) and beyond, including sixth-generation (6G) wireless networks, is driven by demanding use cases such as ultra-reliable low-latency communications (URLLC), immersive extended reality (XR), and high-capacity connectivity at millimeter-wave (mmWave), sub-terahertz (sub-THz), and terahertz (THz) bands. Meeting these ambitious requirements calls for disruptive technologies capable of overcoming the inherent limitations of conventional communication paradigms [3]. However, realizing such goals is significantly hindered by multipath fading, which becomes particularly severe in dense urban deployments and high-frequency regimes where signals traverse multiple propagation paths before reaching the receiver. This phenomenon degrades both signal quality and system reliability, highlighting the critical importance of accurate fading models and robust system design for enabling next-generation wireless networks [4].

In this context, Reconfigurable Intelligent Surfaces (RIS) have emerged as a transformative paradigm by enabling the manipulation of the wireless environment itself rather than merely adapting to it. By programming the electromagnetic response of nearly passive reflecting elements, RIS can steer, focus, or scatter signals in a highly flexible manner, thereby creating favorable propagation conditions on demand [5, 6]. Compared to traditional solutions such as massive MIMO [7] or active relaying [8, 9], RIS provides a cost-effective and energy-efficient alternative that can be seamlessly integrated into existing infrastructure [10]. These advantages make RIS a cornerstone technology for beyond-5G and 6G systems, especially at mmWave and sub-THz bands where establishing reliable links is often challenged by severe blockages and harsh propagation conditions [11]. By dynamically reconfiguring the propagation environment, RIS can improve coverage, mitigate

fading, and substantially enhance communication reliability [12, 13].

Despite the growing interest in RIS technology, most performance analyses still rely on classical fading models such as Rayleigh, Rician, and Weibull [14, 15, 16, 6]. Although these models offer analytical convenience, they fail to accurately capture the intricate propagation dynamics observed at higher frequencies. In particular, mmWave, sub-THz, and THz bands are characterized by unique phenomena, such as severe blockages, pronounced clustering, and dominant line-of-sight (LoS) components, that demand more flexible and representative statistical modeling approaches.

To address these challenges, generalized fading models such as the κ-μ and the Fluctuating Two-Ray (FTR) distributions have been proposed, providing enhanced flexibility for accurately characterizing a wide range of fading conditions [17, 18]. These models facilitate more precise assessments of RIS-assisted systems in next-generation scenarios, highlighting the need to move beyond traditional modeling assumptions [19, 20, 21]. For instance, in [19], exact expressions for the probability density function (PDF) and cumulative distribution function (CDF) of mixed products of generalized fading distributions such as α-μ, κ-μ, and extended η-μ are provided as powerful tools for performance analysis in RIS-assisted communication systems. In [20], a mmWave wiretap scenario with RIS assistance is studied, focusing on secrecy performance under colluding eavesdroppers and introducing a unified framework for FTR and Independent Fluctuating Two-Ray (IFTR) fading models.

While these contributions are significant, deriving analytical expressions under generalized fading models often leads to considerable mathematical complexity and increased computational demands. For example, in [19], performance metrics are expressed through product series whose complexity scales with the number of RIS elements, making analysis infeasible for large configurations. Similarly, in [20], secrecy metrics require the evaluation of Laguerre polynomial expansions, which limits tractability. These challenges emphasize the need for simplified yet accurate analytical frameworks for RIS-assisted systems under generalized fading.

Motivated by this, the multi-cluster fluctuating two-ray (MFTR) fading model has been recently introduced [22]. Building upon the foundations of the FTR and κ-μ shadowed models [23], the MFTR model integrates multiple multipath clusters with fluctuating specular components, providing enhanced versatility for modeling complex propagation environments [24]. Its PDF can reproduce diverse fading behaviors—including bimodality under certain conditions—and unifies a wide family of distributions, including Rayleigh, Rician, Nakagami-m, Hoyt, TWDP, and FTR, within a single analytical framework. This makes MFTR especially suitable for mmWave, sub-THz, and THz communications.

However, to the best of our knowledge, RIS-assisted communication systems have not yet been analyzed under the MFTR model, despite its strong relevance to next-generation wireless scenarios. This omission motivates the present work, which develops new analytical results for RIS-assisted systems over MFTR fading channels, focusing on fundamental performance metrics. By leveraging MFTR, a more refined analysis of RIS performance can be achieved, providing crucial insights into how RIS can be effectively deployed in dynamic and challenging propagation environments. This is particularly important in mmWave scenarios, where channels are highly sensitive to mobility and environmental variations. Accordingly, this work seeks to address the central question: How does a RIS-assisted communication system perform under MFTR fading?

Furthermore, this study extends the analysis by incorporating Signal Space Diversity (SSD), which is designed to mitigate the effects of small-scale fading and diversity loss, rather than large-scale path loss. In high-frequency communications, such as mmWave and THz bands, the dominant impairments are the severe path loss and sensitivity to blockage, which are effectively addressed by Reconfigurable Intelligent Surfaces (RIS) through passive beam steering and coverage enhancement. In contrast, SSD operates at the modulation level and aims to improve robustness against deep fading events by exploiting multidimensional signal-space diversity.

In this context, RIS and SSD play distinct yet complementary roles. RIS enhances the average received signal power and spatial diversity by shaping the propagation envi-

ronment, while SSD improves the reliability of symbol detection under residual fading by ensuring that the transmitted symbols experience independent fading components. This complementarity makes SSD particularly relevant in mmWave scenarios, where, despite RIS-assisted power gains, the channel may still exhibit strong amplitude fluctuations due to sparse scattering and specular component variability.

Although SSD has demonstrated performance gains in RIS-assisted systems under fading models such as Nakagami-m [25], its integration with RIS under the more general MFTR fading model remains unexplored. Investigating this combination therefore opens a novel research direction, highlighting how signal-domain diversity (SSD) can complement propagation-domain control (RIS) to jointly enhance robustness and reliability in severe high-frequency fading environments, while also introducing new analytical challenges associated with generalized fading models.

1.2 Objectives

1.2.1 General Objective

To evaluate, through theoretical analysis and MATLAB-based simulations, the impact of Reconfigurable Intelligent Surfaces on the performance of wireless communication systems operating under Multi-cluster Fluctuating Two-Ray fading channels, using various performance metrics.

1.2.2 Specific Objectives

- Perform a comprehensive literature review to understand study techniques and identify gaps in current knowledge.
- Analyze the performance of a RIS-assisted communication system under the MFTR

fading model through both mathematical modeling and MATLAB-based simulations.

- Generate and interpret curves of various performance metrics by adjusting system parameters to determine optimal operating conditions.
- Investigate and evaluate advanced techniques to further improve RIS-assisted communication system performance, utilizing Monte Carlo simulations.
- To verify through MATLAB simulations the potential performance improvement obtained by incorporating Signal Space Diversity (SSD) into a RIS-assisted wireless communication system under MFTR fading.

1.3 Document Structure

This dissertation is structured into five chapters, each addressing a key aspect of the analysis and evaluation of RIS-assisted wireless communication systems under the MFTR fading model: Chapter 1 outlines the motivation, objectives, and key contributions, highlighting the importance of analyzing RIS-assisted wireless communication systems under the multi-cluster fluctuating two-ray fading model and investigating the incorporation of signal space diversity through simulations. Chapter 2 provides the theoretical foundation on wireless fading channels, RIS principles, and the MFTR model, emphasizing the current gap in studies of RIS-assisted systems under this fading condition. Chapter 3 develops the mathematical framework, deriving both exact and approximate analytical expressions for outage probability (OP), average bit error probability (ABEP), and ergodic capacity of RIS-assisted systems subject to MFTR fading. Chapter 4 validates these analytical findings via simulations and explores the RIS–SSD–MFTR scenario, demonstrating the effectiveness of SSD in improving system robustness. Finally, Chapter 5 concludes the dissertation by summarizing the main results and suggesting future research directions,

including multi-user scenarios, correlated fading environments, and experimental verification.

2 THEORETICAL FRAMEWORK

Wireless channel propagation is governed by random fluctuations that impact system performance. These variations are conventionally categorized into large-scale effects (path loss and shadowing), which define average coverage over long distances, and small-scale effects (multipath fading), which cause rapid, instantaneous signal fluctuations over short spatial/temporal/frequency scales. This chapter establishes the theoretical foundation of the study, presenting the fundamental principles of wireless channel modeling and statistical fading characterization required for the analysis of RIS-assisted communication systems under the MFTR fading model.

2.1 Propagation Phenomena and Why Fading in "Small-Scale"

The wireless channel constitutes one of the most challenging media for reliable and high speed communication due to its inherent variability and sensitivity to environmental factors. The transmitted signal experiences several propagation mechanisms such as reflection, diffraction, and scattering that modify its amplitude and phase as it travels from the transmitter to the receiver [1]. These variations in received power can be classified into two major categories: large-scale and small-scale effects.

In this work, the analysis focuses specifically on small-scale fading effects, as they dominate the instantaneous performance of wireless links in high-frequency scenarios such as millimeter-wave systems. Moreover, the proposed RIS-assisted architecture operating under MFTR fading is primarily influenced by multipath propagation and the statistical characteristics of fast channel variations.

2.1.1 Small-Scale Fading

As illustrated in Fig. 2.1, the long-term average path loss determines the general decay trend of received power with distance, while shadowing introduces slow fluctuations

around this trend. Superimposed on both are the rapid variations caused by small-scale fading.

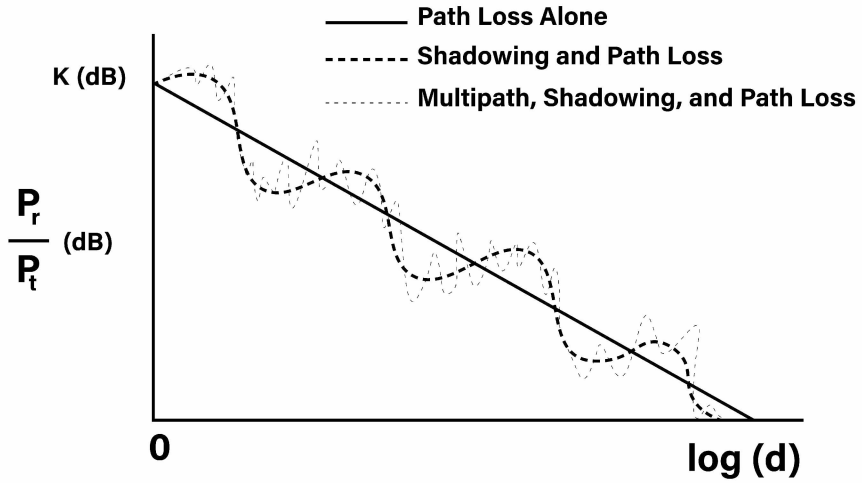

Figure 2.1: Path loss, shadowing, and multipath fading effects versus distance [1].

Small-scale fading represents the rapid fluctuations of the received signal amplitude, phase, and envelope power that occur over very short spatial or temporal intervals, typically on the order of a few wavelengths. In high-frequency systems such as 5G FR2 and beyond, operating at carrier frequencies above 20 GHz, the corresponding wavelengths are on the order of a few centimeters or even millimeters. Consequently, small displacements of the transmitter, receiver, or surrounding objects on the scale of centimeters can produce significant variations in the received signal, making small-scale fading particularly pronounced in mmWave and sub-THz propagation environments. These variations arise from the multipath nature of wireless propagation, in which multiple replicas of the transmitted signal reach the receiver after undergoing reflection, diffraction, and scattering from surrounding objects such as buildings, vehicles, or terrain irregularities [1]. Each propagation path has a distinct amplitude, phase, and delay, and the superposition of these components at the receiver produces constructive and destructive interference. Consequently, even small movements of the transmitter, receiver, or surrounding objects can lead to significant variations in the received power.

Depending on the propagation conditions, the envelope of the received signal can be modeled using different statistical distributions. In the absence of a dominant line-of-sight

(LOS) component, the in phase and quadrature components are modeled as independent zero mean Gaussian random variables, resulting in a Rayleigh distribution for the envelope. When a strong LOS path is present, the amplitude follows a Rician distribution, characterized by the K-factor, which represents the ratio between the power of the deterministic component and the scattered ones. More generally, the Nakagami-m distribution provides a flexible approximation for a wide range of fading severities, where the parameter m controls the fading depth: $m = 1$ corresponds to Rayleigh fading, and higher values indicate less severe fading conditions.

These effects, collectively known as small-scale fading, represent the fine grained temporal and spatial variability of the wireless channel that must be statistically modeled to evaluate the performance of modern communication systems, including those assisted by RIS.

2.1.2 Performance Metrics under Fading

As previously mentioned, the instantaneous quality of a wireless link is strongly influenced by random variations of the received signal power due to fading. As a result, key system performance measures must be statistically characterized rather than treated as deterministic quantities. Among the most fundamental metrics for evaluating link performance are the *outage probability* (OP), the *average bit error probability* (ABEP), and the *ergodic capacity*. These quantities allow the comparison of different channel models and system configurations in terms of reliability, error performance, and achievable data rates.

Let γ denote the instantaneous received signal-to-noise ratio (SNR), which is a random variable that depends on the fading characteristics of the channel. Its probability density function (PDF), $p_\gamma(\gamma)$, captures the statistical behavior of the received SNR over time or space. Using this PDF, one can define performance metrics that provide meaningful averages over many realizations of the fading process.

Outage Probability

The OP quantifies the likelihood that the instantaneous SNR falls below a minimum threshold γ_{th} required to sustain a target data rate or quality of service. It is a measure of link reliability under fading and is expressed as

$$P_{\text{out}} = \Pr(\gamma < \gamma_{\text{th}}) = \int_0^{\gamma_{\text{th}}} p_\gamma(\gamma)\, d\gamma, \tag{2.1}$$

where the integral represents the cumulative distribution function (CDF) of the SNR evaluated at γ_{th}. A lower outage probability implies a more robust link, particularly important in systems targeting ultra-reliable communication such as industrial or vehicular networks [1].

Average Bit Error Probability

The ABEP measures the expected fraction of bits incorrectly detected due to noise and fading. In an additive white Gaussian noise (AWGN) channel, the bit error probability $P_e(\gamma)$ for a given modulation (e.g., BPSK, QPSK, or M-QAM) is a deterministic function of the SNR. Under fading conditions, however, γ varies randomly, and the average error probability is obtained by taking the expectation over its probability distribution, as

$$\overline{P_e} = \int_0^{\infty} P_e(\gamma)\, p_\gamma(\gamma)\, d\gamma. \tag{2.2}$$

This metric captures both the effects of noise and the severity of fading; as the channel becomes more dispersive (e.g., lower m in Nakagami-m or lower μ in κ–μ models), the ABEP increases, indicating degraded reliability [26]. In practice, ABEP curves are often plotted as a function of the average SNR to compare the performance of different fading models or modulation schemes. Starting from the same average SNR, distinct fading distributions lead to different degrees of dispersion in the instantaneous SNR probability density function, which directly impacts the likelihood of deep fades. In turn, the

modulation format determines how these instantaneous SNR variations are mapped into symbol and bit error probabilities. As a result, ABEP curves jointly reflect the influence of the fading severity through the statistical spread of the SNR and the sensitivity of the chosen modulation scheme to noise and fading effects.

Ergodic Capacity

The ergodic capacity defines the maximum achievable average data rate (in bits per second per hertz) that can be transmitted reliably over a fading channel with perfect channel state information (CSI) at the receiver. It represents the long-term average of the instantaneous Shannon capacity over the fading distribution:

$$C_{\text{erg}} = \mathbb{E}[B \log_2(1+\gamma)] = \int_0^\infty B \log_2(1+\gamma)\, p_\gamma(\gamma)\, d\gamma, \tag{2.3}$$

where B is the system bandwidth. The ergodic capacity increases with the average SNR but depends strongly on the fading distribution; for instance, channels with higher diversity (larger μ or m) yield higher capacity for the same average power. This metric is fundamental for evaluating the spectral efficiency of fading channels and is particularly relevant in broadband systems where the channel variations can be averaged over many symbols [27, 1].

Together, these metrics provide a comprehensive view of system behavior under fading conditions. OP reflects the reliability of maintaining a link, ABEP represents the transmission accuracy, and ergodic capacity characterizes the achievable data throughput. In later sections, these expressions will be evaluated under classical and generalized fading models particularly the MFTR distribution to quantify the impact of channel characteristics and RIS-assisted architectures on overall communication performance.

2.2 Generalized Fading Models

The shift toward higher frequency bands, namely mmWave (24–100 GHz), sub-THz (100–300 GHz), and THz (300 GHz–10 THz) is driven by the growing demand for ultra-high data rates in 5G and 6G networks. However, classical models (Rayleigh, Rician) often fail to capture the dominant yet *fluctuating* specular components, sparse scattering, and blockages typical of these bands [1, 28]. Shadowed/generalized models, e.g., κ–μ shadowed, offer more realistic parametric control of LOS dominance, clustering, and fluctuations [23].

2.2.1 The κ–μ, η–μ, and κ–μ Shadowed Models

These families introduce parameters that explicitly encode the number of clusters, LOS dominance, and shadowing, thereby generalizing classical models.

κ–μ Model

The κ–μ model characterizes a fading environment consisting of μ clusters of multipath waves, where each cluster may contain a dominant component. The parameter κ denotes the ratio of dominant to diffuse power [28]. For the instantaneous SNR γ with mean value $\bar{\gamma}$, a commonly used form of the PDF is

$$f_\gamma(\gamma) = \frac{\mu^\mu(1+\kappa)^\mu}{\Gamma(\mu)\,\bar{\gamma}^\mu}\left(\frac{\gamma}{\bar{\gamma}}\right)^{\mu-1}\exp\!\left(-\frac{\mu(1+\kappa)}{\bar{\gamma}}\,\gamma\right) I_{\mu-1}\!\left(2\mu\sqrt{\frac{\kappa(1+\kappa)}{\bar{\gamma}}\,\gamma}\right), \tag{2.4}$$

where $I_\nu(\cdot)$ is the modified Bessel function of the first kind, and $\Gamma(\cdot)$ denotes the Gamma function, defined for $x > 0$ as $\Gamma(x) = \int_0^\infty t^{x-1}e^{-t}\,dt$ [29, eq. (6.1.1)]. Using the results in [28], the CDF of the κ–μ fading model can be expressed in closed form through the generalized Marcum–Q function. Specifically, letting $\bar{\gamma}$ denote the average SNR, the CDF of the instantaneous SNR γ is given by

$$F_\gamma(\gamma) = 1 - Q_\mu\!\left(\sqrt{2\kappa\mu},\,\sqrt{\frac{2(1+\kappa)\mu}{\bar{\gamma}}\,\gamma}\right), \tag{2.5}$$

where $Q_\mu(\cdot,\cdot)$ is the generalized Marcum–Q function. This representation enables tractable evaluation of key performance metrics such as outage probability and bit error probability under κ–μ fading.

η–μ Model

The η–μ model is suitable for representing non-circular scattering conditions, where the in-phase and quadrature components within each cluster have unequal powers [28]. For the envelope R, a commonly used probability density function is given by

$$p_R(r) = \frac{4\mu^\mu}{\Gamma(\mu)} \left(\frac{1+\eta}{1-\eta}\right)^\mu \frac{r^{2\mu-1}}{\Omega^\mu} \exp\left(-\frac{2\mu(1+\eta)}{(1-\eta)\Omega}\, r^2\right) I_{\mu-1}\left(\frac{4\mu\sqrt{\eta}}{(1-\eta)\Omega}\, r^2\right), \quad r \geq 0, \quad (2.6)$$

with $\Omega = \mathbb{E}[R^2]$. Mapping to SNR via $\gamma = \rho\, r^2$ (for some scaling ρ) yields $f_\gamma(\gamma) = \frac{1}{2\sqrt{\rho\gamma}}\, p_R\big(\sqrt{\gamma/\rho}\big)$.

κ–μ Shadowed Model

The κ–μ shadowed model accounts for shadowing on the dominant components of κ–μ fading and admits compact closed-form statistical characterizations [23]. It extends the classical κ–μ model by introducing a fluctuation parameter m that models the random variations affecting the dominant specular waves. When $m \to \infty$, the shadowing effect vanishes, and the model reduces to the standard κ–μ distribution. Conversely, small values of m capture strong shadowing on the LOS components.

For the instantaneous SNR γ, with mean value $\bar{\gamma}$, the probability density function (PDF) is given by [23]:

$$f_\gamma(\gamma) = \frac{\mu^\mu\, m^m (1+\kappa)^\mu}{\Gamma(\mu)\,(\mu\kappa+m)^m\, \bar{\gamma}^\mu}\, \gamma^{\mu-1} \exp\left(-\frac{\mu(1+\kappa)}{\bar{\gamma}}\, \gamma\right)\, {}_1F_1\left(m; \mu; \frac{\mu^2\kappa(1+\kappa)}{(\mu\kappa+m)\bar{\gamma}}\, \gamma\right), \quad (2.7)$$

where ${}_1F_1(\cdot)$ is the confluent hypergeometric function of the first kind.

The CDF also admits a closed-form expression in terms of the Gauss hypergeometric

function:

$$F_\gamma(\gamma) = 1 - \left(\frac{m}{m+\mu\kappa}\right)^m \left(\frac{\mu(1+\kappa)}{\mu(1+\kappa)+\frac{\bar{\gamma}}{\gamma}}\right)^\mu {}_2F_1\left(m,\mu;1+\mu;\frac{\mu\kappa}{m+\mu\kappa}\left(1+\frac{\mu(1+\kappa)\gamma}{\bar{\gamma}}\right)^{-1}\right). \tag{2.8}$$

A particularly useful characterization for performance evaluation is the moment-generating function (MGF), which enables closed-form analysis of metrics such as average bit error probability and ergodic capacity. The MGF of the κ–μ shadowed SNR is given by:

$$M_\gamma(s) = \left(\frac{m}{m+\kappa\mu}\right)^m \left(1+\frac{\bar{\gamma}}{\mu(1+\kappa)}\,s\right)^{-\mu} {}_2F_1\left(m,\mu;1;\frac{\kappa\mu}{m+\kappa\mu}\,\frac{1}{1+\frac{\bar{\gamma}}{\mu(1+\kappa)}s}\right). \tag{2.9}$$

Together, (2.7)–(2.9) demonstrate that the κ–μ shadowed model provides analytically tractable expressions for all key statistical functions of the SNR (PDF, CDF, MGF). This mathematical tractability, combined with its physical relevance, makes the κ–μ shadowed distribution one of the most widely used generalized fading models for characterizing millimeter wave and small-scale fading channels.

2.2.2 Fluctuating Two-Ray (FTR) Model

The FTR model generalizes the Two-Wave with Diffuse Power (TWDP) model by allowing the two specular components to *fluctuate* in amplitude and phase, while including a diffuse component that accurately characterizes high-frequency channels with unstable line-of-sight (LOS) conditions [22]. A tractable characterization of the SNR probability distribution can be obtained using an infinite, fast-converging Gamma mixture, given by

$$f_\gamma(\gamma_{\mathrm{FTR}}) = \sum_{j=0}^{\infty} w_j \,\frac{(j+\mu)^{\,j+\mu}}{\Gamma(j+\mu)\,\bar{\gamma}^{\,j+\mu}}\,\gamma^{\,j+\mu-1}\exp\left(-\frac{(j+\mu)}{\bar{\gamma}}\,\gamma_{\mathrm{FTR}}\right), \tag{2.10}$$

where γ_{FTR} is the SNR under FTR fading and the weights w_j depend on the FTR parameters (K,Δ,m) and satisfy $\sum_{j\geq 0} w_j = 1$. From (2.10):

$$F_\gamma(\gamma_{\mathrm{FTR}}) = \sum_{j=0}^{\infty} w_j \, \frac{\gamma\left(j+\mu, \, \frac{(j+\mu)\gamma_{\mathrm{FTR}}}{\bar{\gamma}}\right)}{\Gamma(j+\mu)}, \tag{2.11}$$

$$M_\gamma(s) = \sum_{j=0}^{\infty} w_j \, \left(1 + \frac{\bar{\gamma}}{j+\mu}\, s\right)^{-(j+\mu)}, \tag{2.12}$$

where $\gamma(\cdot,\cdot)$ is the lower incomplete Gamma function.

2.2.3 The Multi-Cluster Fluctuating Two-Ray (MFTR) Model

Definition and Statistical Characterization

The Multi-Cluster Fluctuating Two-Ray (MFTR) model generalizes the classical FTR distribution by explicitly accounting for the presence of multiple scattering clusters in the propagation environment. Physically, MFTR describes a scenario in which the received signal is formed by the superposition of a small number of dominant specular components and a large number of diffuse scattered waves. In particular, the first cluster contains two strong specular components whose amplitudes fluctuate randomly due to shadowing and environmental dynamics, while the remaining $\mu - 1$ clusters represent groups of weaker multipath components generated by reflections, diffraction, and scattering from surrounding objects. This structure closely matches the propagation characteristics observed in dense urban environments and high-frequency bands, where line-of-sight (LOS) components are often present but subject to instability and blockage.

The fading behavior of the MFTR model is governed by four physically meaningful parameters (μ,m,K,Δ), each linked to a specific propagation mechanism. The parameter μ represents the number of multipath clusters and is directly associated with the richness of the scattering environment; larger values of μ correspond to increased multipath diversity. The parameter m controls the severity of the random fluctuations affecting the dominant specular components, modeling shadowing effects on the LOS paths—small

values of m indicate strong amplitude variability, while the limit $m \to \infty$ corresponds to non-fluctuating, deterministic specular components. The parameter K quantifies the average power ratio between the dominant specular components and the diffuse multipath contribution, reflecting the relative strength of the LOS paths with respect to the scattered field. Finally, the similarity factor Δ captures the power imbalance between the two dominant specular components in the first cluster, ranging from a single effective specular ray ($\Delta = 0$) to two equally strong specular contributions ($\Delta = 1$).

Through this parametric structure, the MFTR model provides an intuitive and flexible physical interpretation of small-scale fading, enabling the modeling of a wide spectrum of propagation conditions, from severe non-line-of-sight scenarios to environments with fluctuating but dominant LOS components, which are characteristic of mmWave and sub-THz wireless systems.

Relationships to Classical and Generalized Distributions

The MFTR model constitutes a unified and highly flexible fading framework that generalizes a wide family of classical and generalized small-scale fading models. Specifically, it extends the traditional FTR distribution by incorporating multiple scattering clusters and stochastic fluctuations on the dominant specular components. This multi-cluster configuration enables the MFTR model to capture the physical characteristics of realistic wireless channels operating at mmWave, sub-THz, and THz bands, where multiple reflection and scattering clusters coexist with a few dominant LOS paths [22].

In its most general form, the MFTR distribution includes several well-known fading models as special cases through appropriate parameter selection, as shown in Table 2.1. When the number of clusters $\mu = 1$, the model reduces to the standard FTR distribution, representing a single-cluster propagation scenario dominated by two fluctuating LOS components and a diffuse background. Moreover, when the similarity factor $\Delta \to 0$ indicating that one of the specular components becomes negligible, or when the fluctuation parameter $m \to \infty$, meaning the amplitudes of the dominant components cease to fluctu-

Table 2.1: Special cases of the MFTR fading model under limiting conditions.

Resulting distribution	**Limiting condition**	**Parameter constraint**
FTR	$\mu = 1$	–
κ–μ Shadowed	$\Delta \to 0$ or $m \to \infty$	–
κ–μ	$m \to \infty$	–
Rician	$\mu = 1$	$\kappa > 0$
Nakagami-m	$\kappa \to 0$	–
Rayleigh	$m = 1$	$\kappa \to 0$

ate, the MFTR model converges to the κ–μ shadowed distribution. This particular model accounts for the shadowing of the dominant components while preserving the clustering behavior of the multipath field.

Additionally, by setting $\mu = 1$ and removing amplitude fluctuations (i.e., $m \to \infty$, $\Delta = 0$), the MFTR reduces to the κ–μ model, which in turn encompasses the Rician and Nakagami-m distributions as special cases when $\mu = 1$ and $\kappa \to 0$, respectively. The Rayleigh distribution is also recovered as a limiting case of Nakagami-m when $m = 1$. These relationships can be summarized in Table. 2.1.

This hierarchical relationship demonstrates the unifying nature of the MFTR model, which can emulate a wide variety of propagation conditions from severe NLoS to lightly shadowed LOS environments by adjusting a small set of physically interpretable parameters. As such, MFTR provides a more general statistical representation capable of modeling realistic fading conditions in next-generation communication systems.

Statistical Properties

The statistical characterization of the MFTR fading model enables analytical tractability while preserving physical interpretability. One of its key advantages is that its envelope power, or equivalently its instantaneous SNR, can be expressed as a convergent weighted mixture of Gamma distributions. This representation is mathematically convenient and numerically stable, enabling efficient evaluation of key performance metrics such as OP, ABEP, and ergodic capacity.

The PDF of the envelope power Y, considering the MFTR fading model, is given

by

$$f_Y(y) = \sum_{i=0}^{\infty} \omega_i \frac{\lambda_i^{\lambda_i}}{\Gamma(\lambda_i)\, v_i^{\lambda_i}} y^{\lambda_i - 1} \exp\left(-\frac{\lambda_i}{v_i} y\right), \qquad \sum_{i=0}^{\infty} \omega_i = 1, \tag{2.13}$$

where ω_i, λ_i, and v_i denote the mixture weight, shape parameter, and scale parameter of the i-th Gamma component, respectively. These coefficients are deterministic functions of the physical parameters (μ, m, K, Δ) of the MFTR model, and can be obtained through recursive or closed form expressions derived in [22]. The mixture form in (2.13) ensures that $f_Y(y)$ is properly normalized and convergent for all feasible parameter values.

From (2.13), other fundamental statistical functions can be derived in closed form. The cumulative distribution function (CDF) can be expressed as

$$F_Y(y) = \sum_{i=0}^{\infty} \omega_i \frac{\gamma\left(\lambda_i, \frac{\lambda_i}{v_i} y\right)}{\Gamma(\lambda_i)}, \tag{2.14}$$

where $\gamma(\cdot,\cdot)$ is the lower incomplete Gamma function. This expression allows direct computation of outage probability and reliability-related measures.

Similarly, the MGF of Y, essential for deriving average performance metrics in closed form, is given by

$$M_Y(s) = \sum_{i=0}^{\infty} \omega_i \left(1 + \frac{v_i}{\lambda_i} s\right)^{-\lambda_i}. \tag{2.15}$$

The MGF representation in (2.15) is particularly useful because it simplifies the derivation of average error probabilities and capacity expressions through standard integration frameworks. For instance, ABEP can be evaluated by integrating the conditional error probability over the MGF domain, while ergodic capacity can be expressed as an expectation involving $M_Y(s)$.

Equations (2.13)–(2.15) collectively form the analytical backbone for the performance analysis of RIS-assisted systems under MFTR fading. The mixture based formalism not only ensures numerical stability and convergence but also provides the flexibility to model a wide range of propagation phenomena encountered in high frequency wireless environments. Consequently, the MFTR model serves as a comprehensive and physically

grounded framework for accurately assessing the performance of modern communication systems operating under complex fading conditions.

2.3 Reconfigurable Intelligent Surfaces (RIS)

A **RIS** is a planar metasurface composed of a large number of low-cost, nearly passive reflecting elements. Each element can independently adjust the phase shift (and possibly the amplitude) of an incident electromagnetic wave, enabling the control of the propagation environment [30, 31]. Unlike a simple mirror, an RIS acts as a software defined reflector: it does not use power amplifiers for retransmission, but instead shapes the reflected wavefront by properly setting the phase shifts of its elements.

Mathematically, the received signal at a user equipment (UE), after reflection by an RIS, can be modeled as

$$\mathbf{y} = (\mathbf{H}_{RU}\mathbf{\Phi}\mathbf{H}_{TR} + \mathbf{H}_{TU})\,\mathbf{x} + \mathbf{n}, \tag{2.16}$$

where:

- $\mathbf{H}_{TR}$ is the channel matrix from the transmitter (Tx) to the RIS.
- $\mathbf{\Phi} = \text{diag}\left(e^{j\phi_1}, e^{j\phi_2}, \ldots, e^{j\phi_N}\right)$ is the diagonal phase-shift matrix for the N RIS elements.
- $\mathbf{H}_{RU}$ is the channel matrix from the RIS to the UE.
- $\mathbf{H}_{TU}$ is the direct Tx-UE channel matrix (if non-negligible).
- $\mathbf{x}$ is the transmitted signal vector.
- $\mathbf{n}$ is additive noise at the receiver.

The primary design goal is to choose the phase shift matrix $\mathbf{\Phi}$ to maximize a performance metric (e.g. SNR, transmission rate, reliability) at the receiver. This often

involves optimizing over ϕ_1,ϕ_2,...,ϕ_N given knowledge of the channel matrices $\mathbf{H}_{TR}$ and $\mathbf{H}_{RU}$ [31, 30].

RIS represent a transformative technology in wireless communications, offering unique advantages compared to existing solutions such as massive multiple-input multiple-output (MIMO) systems, relays, and active beamforming architectures. Both RIS and MIMO aim to enhance spectral efficiency and spatial diversity; however, MIMO relies on multiple active radio-frequency (RF) chains and complex digital signal processing, while RIS achieves similar spatial benefits through passive reflection. By controlling the phase of incident electromagnetic waves, RIS can improve signal propagation without active transmission, resulting in much lower hardware complexity and energy consumption. This makes RIS a compelling candidate for sustainable, low-power communication networks.

When compared to relays, which actively receive, amplify or decode, and re-transmit signals consuming power and adding noise and delay, RIS operates as a nearly passive surface that reflects incoming signals directly after applying optimized phase shifts. This passive operation significantly reduces energy use and system complexity. However, since RIS does not amplify signals, its performance can diminish in scenarios where the incident signal is weak or when the transmitter–receiver distance is large [30, 31].

Unlike active beamforming systems, which depend on amplifiers and active RF chains to shape transmission beams, RIS performs passive beam shaping by adjusting the reflection properties of its elements. Instead of generating new signals, it redirects existing ones, effectively reconfiguring the propagation environment. This capability allows RIS to complement active beamforming and MIMO systems, extending coverage and improving channel conditions through environment control [30, 32].

The flexibility and low power consumption of RIS make it suitable for a wide range of deployment scenarios. In outdoor urban environments, RIS panels can be mounted on building facades, rooftops, or street infrastructure to redirect signals into shadowed or NLOS regions, thereby enhancing coverage and link reliability in dense areas. Indoors, RIS panels integrated into walls or ceilings can mitigate reflections and blockages caused by

furniture or walls, improving throughput and signal quality. Furthermore, RIS technology can be used to enhance physical-layer security by steering reflected signals toward intended users and away from potential eavesdroppers, effectively increasing secrecy capacity [30]. In Internet of Things (IoT) applications, RIS provides an energy-efficient and low-cost solution for improving connectivity in networks with numerous battery-powered devices.

Despite these promising advantages, several implementation challenges remain. One major difficulty is the acquisition of accurate CSI. Because RIS elements are passive and cannot transmit pilot signals, estimating the cascaded transmitter–RIS–receiver channels ($\mathbf{H}_{TR}$ and $\mathbf{H}_{RU}$) is a complex and resource-intensive task [31]. Moreover, practical RIS hardware imposes quantization limits on the achievable phase shifts, leading to small but significant performance losses compared to ideal continuous-phase control. Synchronization and real-time adaptability also present challenges, especially in mobile environments where users and scatterers are constantly moving. To achieve optimal performance, the RIS must continuously adjust its configuration to follow fast-changing channel conditions, which increases the system's control and computational overhead.

2.4 Signal Space Diversity (SSD)

SSD is an advanced modulation technique originally introduced in [33] to enhance diversity gain in wireless systems without compromising spectral efficiency. The fundamental principle of SSD is based on applying a carefully designed rotation to a multidimensional quadrature amplitude modulation (QAM) constellation, such that any two distinct constellation points differ in as many coordinate components as possible. The achievable diversity order of a multidimensional constellation is defined as the minimum number of coordinates in which any two symbols differ. When the rotation is optimized and the constellation has $\mathcal{D}$ dimensions, the system can theoretically achieve a diversity order equal to $\mathcal{D}$.

The SSD principle illustrated in Fig. 2.2 can be understood by analyzing how fading and noise affect symbol detection in rotated and non-rotated constellations. Consider

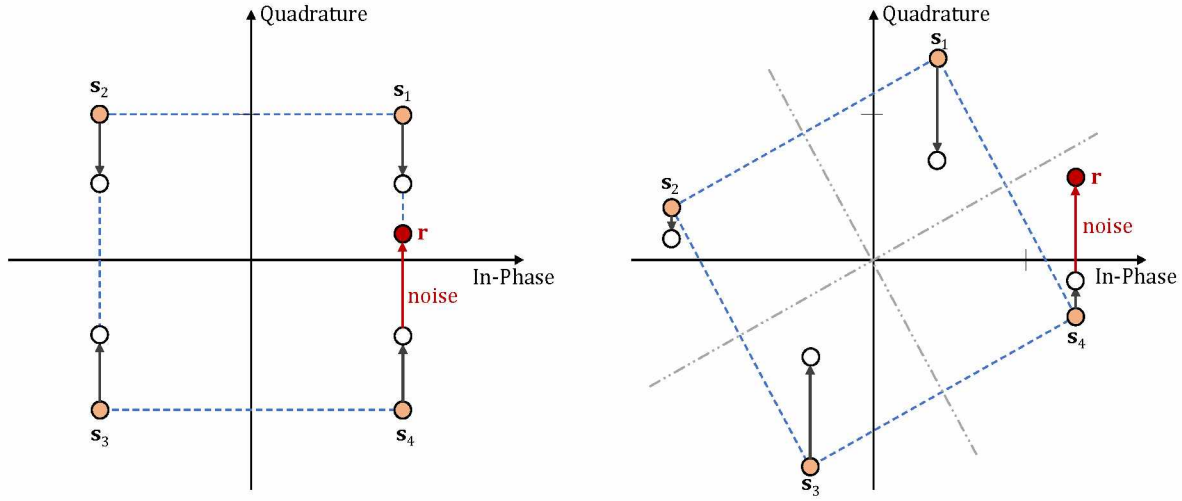

(a) Non-rotated 4-QAM (Diversity order 1).

(b) Rotated 4-QAM (Diversity order 2).

Figure 2.2: SSD principle based on constellation rotation from [2].

first the non-rotated 4-QAM constellation shown on the left. The orange points represent the original constellation symbols. Let us focus on the symbol located in the lower-right quadrant, corresponding to s_4. If a deep fade affects only the quadrature component—as indicated by the black arrow—the symbol is displaced vertically toward the white point. In this situation the in-phase component remains unchanged while the quadrature component is severely attenuated. After this fading-induced displacement, the received sample is further perturbed by additive noise (red arrow), ultimately landing in the upper-right quadrant. As a consequence, the detector incorrectly decides in favor of symbol s_1 instead of the transmitted s_4, illustrating how the lack of rotation causes several constellation points to collapse along the affected axis.

The rotated constellation on the right behaves fundamentally differently. Again consider the transmission of symbol s_4. Although the same fading coefficient is applied, the rotation causes the original quadrature component to have a much smaller magnitude. Thus, the same fading value produces a proportionally smaller displacement in the rotated domain. After fading, the symbol moves toward the corresponding white point. When noise is added (red arrow), the received sample remains within the rotated decision region corresponding to s_4. Since symbol decisions are performed with respect to the rotated axes, the detector correctly identifies the transmitted symbol.

This example illustrates the core advantage of SSD: rotation redistributes the energy of each symbol across both coordinates, preventing any axis-aligned collapse under selective fading. As a result, even when one component is deeply faded, the combined effect of rotation and the multidimensional decision boundaries ensures that the minimum distance between symbols remains nonzero, providing additional diversity and improving detection reliability.

At the transmitter, a block of t bits is mapped into a $\mathcal{D}$-dimensional QAM symbol $\mathbf{s} = (s_1, s_2, ..., s_{\mathcal{D}})^T$, where each component s_ℓ is drawn from the set $\{\pm 1, \pm 3, ..., \pm\sqrt{M}\}$, and transmitted over $\mathcal{D}/2$ time slots (two dimensions per slot). The rotation operation is implemented by multiplying $\mathbf{s}$ by a $\mathcal{D} \times \mathcal{D}$ orthogonal rotation matrix $\mathbf{W}$, yielding the rotated vector $\mathbf{r} = \mathbf{W}^T\mathbf{s}$ [33]. Since $\mathbf{W}$ is orthogonal, the rotation preserves the total transmitted power, ensuring no loss in energy efficiency. The bit rate remains identical to that of a conventional M-QAM system, confirming that SSD introduces no spectral efficiency penalty.

The design of $\mathbf{W}$ plays a critical role in determining system performance. The rotation matrix depends on a set of design parameters, typically denoted by $\lambda_{\mathcal{D}}$, which must be chosen to maximize both the diversity order and the minimum product distance between any two rotated symbols. The product distance, a key metric for assessing performance, is defined as

$$d_p = \prod_{\ell=1}^{\mathcal{D}} |r_{1,\ell} - r_{2,\ell}|, \tag{2.17}$$

where $r_{1,\ell}$ and $r_{2,\ell}$ represent the ℓ-th components of two distinct rotated symbol vectors $\mathbf{r}_1$ and $\mathbf{r}_2$, respectively. Maximizing d_p enhances the system's robustness to fading and noise by increasing the Euclidean distance between symbols in the multidimensional signal space.

The specific rotation matrices for $\mathcal{D} = 2, 3, 4$, and 6 are summarized in Table 2.2. For each dimension, the optimal values for $\lambda_{\mathcal{D}}$ were derived to achieve full diversity and improved SNR performance, with higher-dimensional matrices designed using the recursive procedures outlined in [33].

Table 2.2: Rotation matrices employed with the SSD technique from [2].

$\mathcal{D}$	**Rotation Matrix, W**	**Parameters**
2	$\begin{pmatrix} a & b \\ -b & a \end{pmatrix}$	$a = \frac{1}{\sqrt{1+\lambda_2^2}}$, $b = \lambda_2 a$
3	$\begin{pmatrix} a & b & c \\ b & c & a \\ -c & -a & -b \end{pmatrix}$	$a = \frac{1+\lambda_3}{1+\lambda_3+\lambda_3^2}$, $b = \lambda_3 a$, $c = \frac{-\lambda_3}{1+\lambda_3} a$
4	$\begin{pmatrix} a & b & -c & -d \\ -b & a & d & -c \\ c & d & a & b \\ -d & c & -b & a \end{pmatrix}$	$a = \frac{1}{u\sqrt{1+\lambda_2^2}}$, $b = \frac{\lambda_2}{u\sqrt{1+\lambda_2^2}}$, $c = \frac{\lambda_4}{u\lambda_2}$, $d = \frac{\lambda_4}{u}$ $u = \frac{\sqrt{\lambda_2^2+\lambda_4^4+\lambda_2\lambda_4^2}}{\lambda_2}$
6	$\begin{pmatrix} a & b & c & -x & -y & -z \\ b & c & a & -y & -z & -x \\ -c & -a & -b & z & x & y \\ x & y & z & a & b & c \\ y & z & x & b & c & a \\ -z & -x & -y & -c & -a & -b \end{pmatrix}$	$\dot{a} = \frac{1+\lambda_3}{1+\lambda_3+\lambda_3^2}$, $\dot{b} = \lambda_3 \dot{a}$, $\dot{c} = \frac{-\lambda_3}{1+\lambda_3}\dot{a}$ $\dot{x} = \lambda_6$, $\dot{y} = \frac{\dot{b}-\dot{a}-\sqrt{(\dot{b}-\dot{a})^2+(\dot{a}-\dot{c})(\dot{b}-\dot{c})}}{\dot{a}-\dot{c}}\dot{x}$, $\dot{z} = \frac{-\dot{x}\dot{y}}{\dot{x}+\dot{y}}$ $u = \sqrt{\dot{a}^2+\dot{b}^2+\dot{c}^2+\dot{x}^2+\dot{y}^2+\dot{z}^2}$ $a = \frac{\dot{a}}{u}$, $b = \frac{\dot{b}}{u}$, $c = \frac{\dot{c}}{u}$, $x = \frac{\dot{x}}{u}$, $y = \frac{\dot{y}}{u}$, $z = \frac{\dot{z}}{u}$

At the receiver, the system first compensates for the phase distortions introduced by the channel and then applies a deinterleaver to separate the faded components. The symbol detection process follows the minimum Euclidean distance criterion:

$$\tilde{\mathbf{r}} = \arg\min_{\hat{\mathbf{r}}} \sum_{\ell=1}^{\mathcal{D}} |y_\ell - \alpha_\ell \hat{r}_\ell|^2, \tag{2.18}$$

where y_ℓ denotes the received signal in the ℓ-th dimension, α_ℓ represents the fading amplitude affecting that dimension, and $\hat{r}_\ell$ is the ℓ-th element of a candidate symbol vector $\hat{\mathbf{r}}$. Once the optimal rotated symbol $\tilde{\mathbf{r}}$ is identified, the corresponding non-rotated multidimensional symbol $\mathbf{s}$ can be reconstructed, allowing the recovery of the transmitted bit sequence.

In essence, SSD introduces controlled geometric rotation in the signal space to exploit multidimensional diversity without sacrificing bandwidth or data rate. This tech-

nique effectively combats the detrimental effects of fading by ensuring that each component of the signal vector carries independent and complementary information, thereby improving the reliability and robustness of wireless transmission systems operating in frequency-selective or multipath fading environments.

The concepts established in this chapter, small-scale fading statistics, generalized models with emphasis on MFTR, core performance metrics (OP, ABEP, and ergodic capacity), and the fundamentals of RIS and SSD provide the analytical substrate for the developments that follow. In the next chapter, *System Model and Performance Analysis*, these ideas are instantiated into a precise baseband framework for an RIS-assisted link under MFTR fading, specifying all channel and path-loss assumptions, as well as the RIS configuration and the SSD mapping/rotation at the transceiver.

3 SYSTEM MODEL AND PERFORMANCE ANALYSIS

3.1 System and Channel Models

We consider a wireless communication system operating under non-line-of-sight (NLoS) conditions and assisted by a RIS, as illustrated in Fig.3.1. The system consists of a single-antenna transmitter, a RIS composed of N passive reflecting elements, and a single-antenna receiver. There is no direct link between the transmitter and the receiver; instead, the RIS reflects the signal towards the receiver, applying programmable phase shifts to enhance reception.

For this system model, the received signal sample can be expressed as

$$\begin{aligned} y &= \sqrt{P_{\mathrm{r}}} \left(\sum_{n=1}^{N} g_n h_n e^{j\theta_n} \right) x + w \\ &= \mathbf{h}^{\mathrm{T}} \boldsymbol{\Theta} \mathbf{g}\, x + w, \end{aligned} \tag{3.1}$$

where

$$P_{\mathrm{r}} = P_{\mathrm{t}} \mathcal{K}_1 d_1^{-\alpha_1} \mathcal{K}_2 d_2^{-\alpha_2}, \tag{3.2}$$

where P_{t} denotes the total transmit power, while d_1 and d_2, $\mathcal{K}_1$ and $\mathcal{K}_2$, and α_1 and α_2 represent the distances, propagation factors, and path-loss exponents associated with the transmitter–RIS and RIS–receiver links, respectively. Furthermore, in (3.1), x denotes the transmitted symbol drawn from a normalized mean power M-QAM constellation, i.e., $E\{x^2\} = 1$, with M representing the constellation size. In addition, $\mathbf{g} = [g_1, g_2, \ldots, g_N]^{\mathrm{T}}$ and $\mathbf{h} = [h_1, h_2, \ldots, h_N]^{\mathrm{T}}$ denote the complex channel vectors associated with the transmitter-to-RIS and RIS-to-receiver links, respectively, with all entries normalized to have unit average power, i.e., $E\{g_n^2\} = E\{h_n^2\} = 1$, $\forall n$. The RIS phase-shift matrix is defined as $\boldsymbol{\Theta} = \mathrm{diag}(e^{j\theta_1}, e^{j\theta_2}, \ldots, e^{j\theta_N})$. Finally, w denotes the complex additive

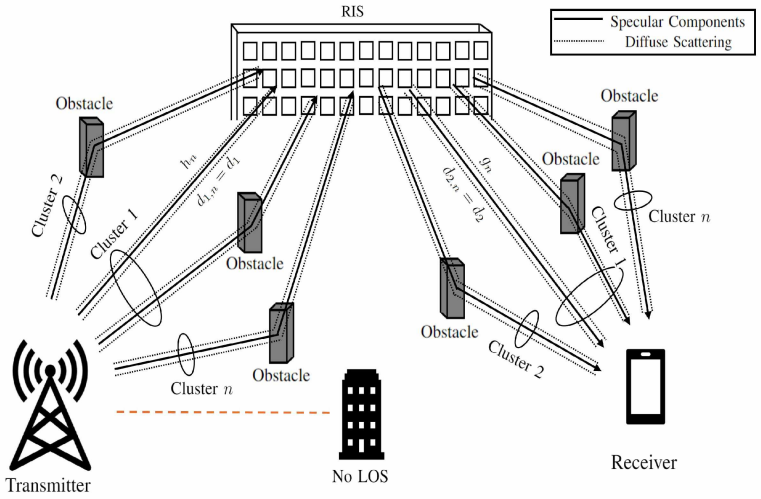

Figure 3.1: RIS-assisted communication system without direct line of sight.

white Gaussian noise sample, such that, $w \sim \mathcal{CN}(0,\sigma_n^2)$.

The fading coefficients $\{g_n\}$ and $\{h_n\}$ are assumed to be independent across the RIS elements and mutually independent between the transmitter–RIS and RIS–receiver links. Within each link, the coefficients are identically distributed, i.e., $\{g_n\}$ and $\{h_n\}$ are modeled as i.i.d. random variables following the MFTR distribution, while the two links may exhibit different fading statistics.

This assumption is physically justified when the RIS elements are sufficiently spaced (typically on the order of half a wavelength) and interact with distinct local scattering environments, leading to uncorrelated fading. Likewise, independence between the two links is reasonable when they are affected by different sets of scatterers, as commonly occurs in practical RIS deployments. Although spatial correlation may arise in compact or highly structured scenarios, the independence assumption provides an accurate and tractable model for system-level performance analysis.

Each fading coefficient in the vectors $\mathbf{g}$ and $\mathbf{h}$ can be modeled using the MFTR distribution [22]. Specifically, the instantaneous power of the n-th MFTR random variable

can be represented as[1]

$$|\rho|^2 = \left|\sqrt{\delta}\left(V_1 e^{j\phi_1} + V_2 e^{j\phi_2}\right) + \mathcal{G}_1\right|^2 + \sum_{u=2}^{\mu}\left|\sqrt{\delta}\, U_u e^{j\psi_u} + \mathcal{G}_u\right|^2, \tag{3.3}$$

for $\rho \in \{g, h\}$, where δ is a Gamma-distributed random variable with unit mean, whose PDF is given by

$$f_{\delta(z)} = \frac{m^m z^{m-1}}{\Gamma(m)} \exp(-mz), \tag{3.4}$$

with $m > 0$ denoting the shadowing severity parameter of the dominant specular waves.

In this model, the first cluster contains two strong specular components with fixed amplitudes V_1 and V_2, and phases $\phi_1, \phi_2 \sim \mathcal{U}[0,2\pi)$. Additional clusters are represented by components of the form $U_u e^{j\psi_u}$, where U_u is constant and $\psi_u \sim \mathcal{U}[0,2\pi)$. Each cluster also includes a diffuse contribution $\mathcal{G}_u \sim \mathcal{CN}(0,2\sigma^2)$, with $u = 1,2,\ldots,\mu$, σ^2 denotes the variance of both the in-phase and quadrature components of $\mathcal{G}_u$ and μ denoting the total number of multipath clusters.

The marginal PDF of $|\rho|^2$ is given in [22, eq. (20)] as

$$f_{|\rho|^2}(y) = \sum_{i=0}^{\infty} \omega_i \frac{\lambda_i^{\lambda_i}}{\Gamma(\lambda_i) v_i^{\lambda_i}} y^{\lambda_i - 1} \exp\left(-\frac{\lambda_i y}{v_i}\right), \tag{3.5}$$

where the weights ω_i are given by

$$\omega_i = \frac{m^m\, \Gamma(m+i)\, (\mu K(1-\Delta))^i}{\sqrt{\pi}\, \Gamma(m)\Gamma(i+1)\, (m+\mu K(1-\Delta))^{m+i}} \times \sum_{q=0}^{i} \binom{i}{q} \frac{\Gamma(q+\frac{1}{2})}{\Gamma(q+1)} \left(\frac{2\Delta}{1-\Delta}\right)^q \times {}_2F_1\left(m+i, q+\tfrac{1}{2}; q+1; -\frac{2\mu K \Delta}{m+\mu K(1-\Delta)}\right). \tag{3.6}$$

[1]We have simplified the notation by omitting the subscript n.

In addition, in (3.5)-(3.6) we have that

$$\lambda_i = \mu + i, \tag{3.7}$$

and that

$$v_i = \frac{\mu + i}{\mu(k + i)}, \tag{3.8}$$

where the parameter

$$K = \frac{V_1^2 + V_2^2 + \sum_{u=2}^{\mu} U_u^2}{2\sigma^2 \mu}, \tag{3.9}$$

quantifies the ratio between the power of the deterministic specular components and that of the diffuse part, whereas

$$\Delta = \frac{2V_1 V_2}{V_1^2 + V_2^2 + \sum_{u=2}^{\mu} U_u^2}, \quad 0 \leq \Delta \leq 1, \tag{3.10}$$

measures the similarity of the dominant specular components in the first cluster.

3.2 Performance Analysis

In this section, we analyze the performance of the proposed RIS-assisted communication system in terms of OP and ABEP by considering M-QAM. The analysis begins with the characterization of the instantaneous received signal-to-noise ratio (SNR), which constitutes the foundation for all subsequent derivations.

3.2.1 Signal-to-Noise Ratio

When the RIS phase shifts in (3.1) are optimally configured as[2]

$$\theta_n^\star = -\arg(g_n h_n), \tag{3.11}$$

each reflected signal undergoes perfect phase compensation. This ensures that the cascaded links $\{h_n g_n\}$ are coherently aligned at the receiver, so that all contributions add constructively. Under this assumption, the received signal can be rewritten as

$$y = \sqrt{P_\mathrm{r}} \underbrace{\sum_{n=1}^{N} |g_n||h_n|}_{r} x + n. \tag{3.12}$$

From this result, the instantaneous received SNR can be expressed as

$$\Psi = \bar{\gamma} r^2, \tag{3.13}$$

where $\bar{\gamma} = P_\mathrm{r}/\sigma_n^2$.

Since the number of RIS elements, N, is typically large, by invoking the Central Limit Theorem [36], the random variable r in (3.12) can be approximated as Gaussian, which enables a tractable characterization of its distribution by capturing the aggregate effect of a large number of independent (or weakly dependent) reflected components. This approximation becomes increasingly accurate as N grows, and is well aligned with practical RIS deployments, while significantly simplifying the derivation of closed-form performance expressions, i.e., $r \sim \mathcal{N}(\eta_r, \sigma_r^2)$. Therefore, its PDF can be written as

$$f_r(y) = \frac{1}{\sqrt{2\pi}\,\sigma_r} \exp\left(-\frac{(y-\eta_r)^2}{2\sigma_r^2}\right), \tag{3.14}$$

[2]By setting $\theta_n^\star$ at each element, all reflected signals are phase-aligned to achieve maximal constructive interference at the receiver. This widely adopted assumption provides an upper bound on system performance and can be reasonably justified, since near-perfect alignment is attainable with accurate CSI estimation or channel reciprocity in wireless systems [34, 31, 35].

for $-\infty < y < \infty$.

Our objective is now to determine η_r and σ_r^2 for this Gaussian distribution, under the assumption that g_n and h_n are independent but not necessarily identically distributed MFTR random variables. To this end, we first derive the PDF of the MFTR envelope $|\rho|$, where $|\rho| \in \{|g|,|h|\}$. Recalling that (3.5) denotes the PDF of the squared MFTR fading envelope, a straightforward change of variables can be applied, yielding

$$f_{|\rho|}(y) = 2\sum_{i=0}^{\infty} \omega_i \frac{\lambda_i^{\lambda_i}}{\Gamma(\lambda_i) v_i^{\lambda_i}} y^{2\lambda_i - 1} \exp\left(-\frac{\lambda_i y^2}{v_i}\right), \tag{3.15}$$

where ω_i, λ_i and v_i are given by (3.6), (3.7), and (3.8), respectively.

Starting from the definition of the expectation of ρ, we have that

$$E[\rho] = \int_0^{\infty} y\, f_{|\rho|}(y)\, dy = \sum_{i=0}^{\infty} \omega_i \frac{\lambda_i^{\lambda_i}}{\Gamma(\lambda_i) v_i^{\lambda_i}} \int_0^{\infty} y^{2\lambda_i} \exp\left(-\frac{\lambda_i}{v_i} y^2\right) dy. \tag{3.16}$$

To express the integral in terms of the Gamma function from [29, eq. (6.1.1)], we apply the following change of variables

$$t = \frac{\lambda_i}{v_i} y^2, \qquad y = \sqrt{\frac{v_i}{\lambda_i}}\, t^{1/2}, \qquad dy = \frac{1}{2}\sqrt{\frac{v_i}{\lambda_i}}\, t^{-1/2} dt.$$

Substituting into the integral:

$$\int_0^{\infty} y^{2\lambda_i} \exp\left(-\frac{\lambda_i}{v_i} y^2\right) dy = \int_0^{\infty} \left(\sqrt{\frac{v_i}{\lambda_i}}\, t^{1/2}\right)^{2\lambda_i} e^{-t} \left(\frac{1}{2}\sqrt{\frac{v_i}{\lambda_i}}\, t^{-1/2}\right) dt \tag{3.17}$$

$$= \frac{1}{2}\left(\frac{v_i}{\lambda_i}\right)^{\lambda_i + \frac{1}{2}} \int_0^{\infty} t^{\lambda_i - \frac{1}{2}} e^{-t}\, dt. \tag{3.18}$$

We now recognize the remaining integral as Euler's Gamma function:

$$\Gamma(z) = \int_0^{\infty} t^{z-1} e^{-t}\, dt, \qquad \Re(z) > 0,$$

with $z = \lambda_i + \frac{1}{2}$. Hence,

$$\int_0^\infty y^{2\lambda_i} \exp\left(-\frac{\lambda_i}{v_i} y^2\right) dy = \left(\frac{\lambda_i}{v_i}\right)^{-\lambda_i - \frac{1}{2}} \Gamma\left(\lambda_i + \tfrac{1}{2}\right).$$

Finally, substituting this result yields to

$$E[\rho] = \sum_{i=0}^{\infty} \omega_i \frac{\lambda_i^{\lambda_i}}{\Gamma(\lambda_i) v_i^{\lambda_i}} \left(\frac{\lambda_i}{v_i}\right)^{-\frac{1}{2}-\lambda_i} \Gamma\left(\frac{1}{2} + \lambda_i\right), \tag{3.19}$$

to (3.19).

Based on this result, the mean value η_r can be derived as

$$\begin{aligned} \eta_r &= E\left\{\sum_{n=1}^{N} |g_n||h_n|\right\} \\ &= \sum_{n=1}^{N} E\{|g_n|\}\, E\{|h_n|\} \\ &= N\, E\{|g|\}\, E\{|h|\}, \end{aligned} \tag{3.20}$$

where, in the final step, it was assumed that all elements of $\mathbf{h}$ and $\mathbf{g}$ are identically distributed, i.e., $E\{|g_n|\} = E\{|g|\}$, and $E\{|h_n|\} = E\{|h|\}$, for all n.

Finally, using the result in (3.19), (3.20) can be rewritten as follows

$$\begin{aligned} \eta_r =& N \sum_{i=0}^{\infty} \omega_{i,1} \frac{\lambda_{i,1}^{\lambda_{i,1}}}{\Gamma(\lambda_{i,1}) v_{i,1}^{\lambda_{i,1}}} \left(\frac{\lambda_{i,1}}{v_{i,1}}\right)^{-\frac{1}{2}-\lambda_{i,1}} \Gamma\left(\frac{1}{2} + \lambda_{i,1}\right) \\ &\times \sum_{j=0}^{\infty} \omega_{j,2} \frac{\lambda_{j,2}^{\lambda_{j,2}}}{\Gamma(\lambda_{j,2}) v_{j,2}^{\lambda_{j,2}}} \left(\frac{\lambda_{j,2}}{v_{j,2}}\right)^{-\frac{1}{2}-\lambda_{j,2}} \Gamma\left(\frac{1}{2} + \lambda_{j,2}\right), \end{aligned} \tag{3.21}$$

where subscripts 1 and 2 refer to the MFTR channel parameters associated with the transmitter-to-RIS and RIS–to-receiver links, respectively.

On the other hand, the variance σ_r^2 can be computed as follows

$$\begin{aligned}\sigma_r^2 &= \mathrm{Var}\left[\sum_{n=1}^{N} |g_n\|h_n|\right] \\ &\overset{(a)}{=} N\mathrm{Var}\left[|g_n||h_n|\right] \\ &\overset{(b)}{=} N\left(E\left[|g_n|^2\right]E\left[|h_n|^2\right] - E^2\left[|g_n||h_n|\right]\right) \\ &\overset{(c)}{=} N\left(1-\theta^2\right), \end{aligned} \tag{3.22}$$

where in step (a), we use that the random variables g_n and h_n are independent for all n; in step (b), we use that $\sigma_x^2 = E[x^2] - E^2[x]$; and in step (c), we use that $E[g_n^2] = E[h_n^2] = 1$, $\forall n$, and that $E[|g_n||h_n|] = \theta$, with η_r given in (3.21).

Since r in (3.12) is approximated by a Gaussian distribution, i.e., $r \sim \mathcal{N}(\eta_r,\sigma_r^2)$, its PDF is given by (3.14). From (3.13), the instantaneous SNR is

$$\Psi = \bar{\gamma}r^2, \qquad \bar{\gamma} = \frac{P_{\mathrm{r}}}{\sigma_n^2},$$

which defines a one–to–two mapping between r and Ψ for $\Psi > 0$. For a given value $y > 0$ of Ψ, the corresponding values of r are

$$r_0(y) = +\sqrt{\frac{y}{\bar{\gamma}}}, \qquad r_1(y) = -\sqrt{\frac{y}{\bar{\gamma}}}.$$

Using the standard transformation rule for a monotonic function with two preimages,

$$f_\Psi(y) = \sum_{k=0}^{1} f_r\big(r_k(y)\big)\left|\frac{dr_k(y)}{dy}\right|, \qquad y > 0,$$

where $f_r(\cdot)$ is given in (3.14). The derivatives of $r_k(y)$ are

$$\frac{dr_k(y)}{dy} = (-1)^k\frac{1}{2\sqrt{\bar{\gamma}y}}, \qquad \left|\frac{dr_k(y)}{dy}\right| = \frac{1}{2\sqrt{\bar{\gamma}y}},$$

which is independent of k. Therefore,

$$f_{\Psi}(y) = \sum_{k=0}^{1} \frac{1}{\sqrt{2\pi}\,\sigma_r} \exp\left(-\frac{(r_k(y)-\eta_r)^2}{2\sigma_r^2}\right) \frac{1}{2\sqrt{\bar{\gamma}y}}$$
$$= \frac{1}{2\sqrt{2\pi\bar{\gamma}\sigma_r^2 y}} \left\{ \exp\left[-\frac{1}{2\sigma_r^2}\left(\sqrt{\frac{y}{\bar{\gamma}}} - \eta_r\right)^2\right] + \exp\left[-\frac{1}{2\sigma_r^2}\left(\sqrt{\frac{y}{\bar{\gamma}}} + \eta_r\right)^2\right] \right\}.$$

This expression can be compactly written as

$$f_{\Psi}(y) = \frac{1}{2\sqrt{2\pi\bar{\gamma}\sigma_r^2 y}} \left\{ \exp\left[-\frac{1}{2\sigma_r^2}\left(\sqrt{\frac{y}{\bar{\gamma}}} + \eta_r\right)^2\right] + \exp\left[-\frac{1}{2\sigma_r^2}\left(\sqrt{\frac{y}{\bar{\gamma}}} - \eta_r\right)^2\right] \right\}$$
$$= \frac{1}{2\sqrt{2\pi\bar{\gamma}\sigma_r^2 y}} \sum_{k=0}^{1} \exp\left[-\frac{1}{2\sigma_r^2}\left(\sqrt{\frac{y}{\bar{\gamma}}} + (-1)^k \eta_r\right)^2\right], \tag{3.23}$$

for $y > 0$, which corresponds to (3.23).

3.2.2 Outage Probability

The OP is defined as the probability that the instantaneous channel capacity falls below a target threshold R_{th}. Equivalently, it can be expressed as

$$P_{\text{out}} = \Pr\left(\log_2(1+\Psi) < R_{\text{th}}\right), \tag{3.24}$$

where Ψ is the instantaneous received SNR given in (3.13). Therefore, the OP can be obtained as follows

$$P_{\text{out}} = \Pr\left(\Psi < 2^{R_{\text{th}}} - 1\right)$$
$$= \int_0^{2^{R_{\text{th}}}-1} f_{\Psi}(y)\mathrm{d}y \tag{3.25}$$

where $f_{\Psi}(y)$ is given in (3.23).

Using (3.23) in (3.25), the OP can be written as

$$\begin{aligned} P_{\text{out}} &= \int_0^{\gamma_{\text{th}}} f_\Psi(y)\, dy \\ &= \int_0^{\gamma_{\text{th}}} \frac{1}{2\sqrt{2\pi\bar{\gamma}\sigma_r^2 y}} \sum_{k=0}^{1} \exp\left[-\frac{1}{2\sigma_r^2}\left(\sqrt{\frac{y}{\bar{\gamma}}} + (-1)^k \eta_r\right)^2\right] dy \\ &= \frac{1}{2\sqrt{2\pi\bar{\gamma}\sigma_r^2}} \sum_{k=0}^{1} \int_0^{\gamma_{\text{th}}} \frac{1}{\sqrt{y}} \exp\left[-\frac{1}{2\sigma_r^2}\left(\sqrt{\frac{y}{\bar{\gamma}}} + (-1)^k \eta_r\right)^2\right] dy. \end{aligned}$$

Now, we perform the change of variable

$$x = \sqrt{\frac{y}{\bar{\gamma}}} \quad \Rightarrow \quad y = \bar{\gamma}x^2, \quad dy = 2\bar{\gamma}x\, dx, \quad \sqrt{y} = \sqrt{\bar{\gamma}}\, x.$$

When y goes from 0 to γ_{th}, x goes from 0 to

$$x_{\text{th}} = \sqrt{\frac{\gamma_{\text{th}}}{\bar{\gamma}}} = \sqrt{\frac{2^{R_{\text{th}}} - 1}{\bar{\gamma}}}.$$

Hence,

$$\begin{aligned} P_{\text{out}} &= \frac{1}{2\sqrt{2\pi\bar{\gamma}\sigma_r^2}} \sum_{k=0}^{1} \int_0^{x_{\text{th}}} \frac{1}{\sqrt{\bar{\gamma}}\, x} \exp\left[-\frac{(x + (-1)^k \eta_r)^2}{2\sigma_r^2}\right] 2\bar{\gamma}x\, dx \\ &= \frac{1}{\sqrt{2\pi}\,\sigma_r} \sum_{k=0}^{1} \int_0^{x_{\text{th}}} \exp\left[-\frac{(x + (-1)^k \eta_r)^2}{2\sigma_r^2}\right] dx. \end{aligned}$$

Next, we map the integral to the standard Gaussian form by defining

$$u = \frac{x + (-1)^k \eta_r}{\sqrt{2}\,\sigma_r} \quad \Rightarrow \quad dx = \sqrt{2}\,\sigma_r\, du.$$

For a fixed k, the integration limits become

$$u_0^{(k)} = \frac{(-1)^k \eta_r}{\sqrt{2}\,\sigma_r}, \qquad u_1^{(k)} = \frac{x_{\text{th}} + (-1)^k \eta_r}{\sqrt{2}\,\sigma_r}.$$

Therefore,

$$P_{\text{out}} = \frac{1}{\sqrt{2\pi}\,\sigma_r} \sum_{k=0}^{1} \int_{u_0^{(k)}}^{u_1^{(k)}} \exp(-u^2)\,\sqrt{2}\,\sigma_r\,du$$
$$= \frac{1}{\sqrt{\pi}} \sum_{k=0}^{1} \int_{u_0^{(k)}}^{u_1^{(k)}} e^{-u^2}\,du.$$

Using the definition of the error function,

$$\text{erf}(x) = \frac{2}{\sqrt{\pi}} \int_0^x e^{-t^2}\,dt,$$

we can write

$$P_{\text{out}} = \frac{1}{2} \sum_{k=0}^{1} \left[\text{erf}\left(u_1^{(k)}\right) - \text{erf}\left(u_0^{(k)}\right) \right].$$

Note that

$$u_0^{(0)} = \frac{\eta_r}{\sqrt{2}\,\sigma_r}, \qquad u_0^{(1)} = -\frac{\eta_r}{\sqrt{2}\,\sigma_r},$$

and since the error function is odd, $\text{erf}(-x) = -\,\text{erf}(x)$, we obtain

$$\text{erf}\left(u_0^{(0)}\right) + \text{erf}\left(u_0^{(1)}\right) = 0.$$

Thus, only the upper limits contribute, and we finally arrive at

$$P_{\text{out}} = \frac{1}{2} \sum_{k=0}^{1} \text{erf}\left(\frac{1}{\sqrt{2}\,\sigma_r} \left(\sqrt{\frac{2^{R_{\text{th}}} - 1}{\bar{\gamma}}} + (-1)^k \eta_r \right) \right), \tag{3.26}$$

which is the desired closed-form expression for the OP.

3.2.3 Average Bit Error Probability

The ABEP can be computed by averaging over the fading distribution, namely

$$P_b = \int_0^\infty P_\Psi(y) f_\Psi(y)\, \mathrm{d}y, \tag{3.27}$$

where $P_\Psi(y)$ represents the bit error probability conditioned on the instantaneous SNR, and $f_\Psi(y)$ is the PDF of the SNR as given in (3.23).

By considering the symmetry of square M-QAM constellations and Gray encoding, in [37, eq. (16)] it is shown that

$$\begin{aligned} P_\Psi(y) = \frac{1}{\sqrt{M}\log_2\sqrt{M}} \sum_{a=1}^{\log_2\sqrt{M}} \sum_{b=0}^{(1-2^{-a})\sqrt{M}-1} (-1)^{\left\lfloor \frac{b2^{a-1}}{\sqrt{M}} \right\rfloor} \\ \times \left(2^{a-1} - \left\lfloor \frac{b2^{a-1}}{\sqrt{M}} + \frac{1}{2} \right\rfloor \right) \operatorname{erfc}\left((2b+1)\sqrt{\frac{y}{w}}\right), \end{aligned} \tag{3.28}$$

where $w = 2(M-1)/3$.

By substituting (3.23) and (3.28) into (3.27), the resulting integral unfortunately does not admit a closed-form solution. Nevertheless, an accurate approximation can be derived by employing the expression for the complementary error function $\operatorname{erfc}(\cdot)$ proposed in [38, eq. (14)]. Specifically, the complementary error function can be approximated as

$$\operatorname{erfc}(y) \approx \frac{1}{6}\exp(-y^2) + \frac{1}{2}\exp\left(-\frac{4y^2}{3}\right). \tag{3.29}$$

By substituting $x = (2b+1)\sqrt{y/w}$ into (3.29), we obtain

$$\operatorname{erfc}\left((2b+1)\sqrt{\frac{y}{w}}\right) \approx \frac{1}{6}\exp\left(-\frac{(2b+1)^2}{w}y\right) + \frac{1}{2}\exp\left(-\frac{4(2b+1)^2}{3w}y\right). \tag{3.30}$$

For compactness, we rewrite (3.30) as

$$\operatorname{erfc}\left((2b+1)\sqrt{\frac{y}{w}}\right) \approx \sum_{k=0}^{1} \alpha_k \exp\big(-\beta_k(2b+1)^2 y\big), \tag{3.31}$$

where

$$\alpha_0 = \frac{1}{6}, \quad \beta_0 = \frac{1}{w}, \qquad \alpha_1 = \frac{1}{2}, \quad \beta_1 = \frac{4}{3w}.$$

Substituting this approximation into (3.28) yields

$$P_\Psi(y) \approx \frac{1}{\sqrt{M}\log_2\sqrt{M}} \sum_{a=1}^{\log_2\sqrt{M}} \sum_{b=0}^{(1-2^{-a})\sqrt{M}-1} (-1)^{\left\lfloor \frac{b2^{a-1}}{\sqrt{M}} \right\rfloor} \times \left(2^{a-1} - \left\lfloor \frac{b2^{a-1}}{\sqrt{M}} + \frac{1}{2} \right\rfloor\right) \sum_{k=0}^{1} \alpha_k \exp\big(-\beta_k(2b+1)^2 y\big).$$

By applying this approximation to (3.28) and subsequently substituting the result into (3.27), a closed-form approximate expression for evaluating the ABEP in an RIS-assisted system operating over MFTR fading channels can be obtained after some manipulations, and it is given by

$$P_b \approx \frac{1}{\sqrt{M}\log_2\sqrt{M}} \sum_{a=1}^{\log_2\sqrt{M}} \sum_{b=0}^{(1-2^{-a})\sqrt{M}-1} (-1)^{\left\lfloor \frac{b2^{a-1}}{\sqrt{M}} \right\rfloor} \times \left(2^{a-1} - \left\lfloor \frac{b2^{a-1}}{\sqrt{M}} + \frac{1}{2} \right\rfloor\right) \exp\left(-\frac{\eta_r^2}{2\sigma_r^2}\right) \times \frac{\sqrt{w\bar{\gamma}\sigma_r^2}}{2} \sum_{k=0}^{1} \zeta_k \frac{\exp\left(\frac{\eta_r^2}{2\sigma_r^2(1+c_k\bar{\gamma}^2\sigma_r^2)}\right)}{\sqrt{(2b+1)^2 c_k \bar{\gamma}^2 \sigma_r^2 + w}}, \tag{3.32}$$

where $\zeta_k = 1 - 2k/3$ and $c_k = 2(1 + k/3)$.

3.3 Signal Space Diversity Integration in the System Model

To further investigate the diversity enhancement capabilities of the proposed RIS-assisted system, SSD was incorporated at the transmitter and receiver stages. Unlike spatial diversity techniques that rely on multiple antennas, SSD introduces diversity directly in the signal domain by rotating the constellation of the modulated symbols across multiple dimensions. This operation ensures that the in-phase and quadrature components of each symbol experience independent fading realizations, thereby improving resilience

against deep fades in the channel.

At the transmitter, the bit stream is first mapped onto an M-QAM constellation using Gray encoding. The resulting symbol vector $\mathbf{s}$ is then multiplied by a rotation matrix $\mathbf{W}$, producing the rotated vector $\mathbf{r} = \mathbf{W}^T\mathbf{s}$. This rotation redistributes the energy of each symbol across multiple components, maximizing the minimum Euclidean and product distances between constellation points. Subsequently, an interleaver rearranges the symbol components across consecutive time slots to ensure that adjacent components are transmitted over independently faded channel instances. The complete process, depicted in Fig. 3.2, illustrates the transmit processing chain, which consists of three main blocks: the mapper, the rotation block, and the interleaver.

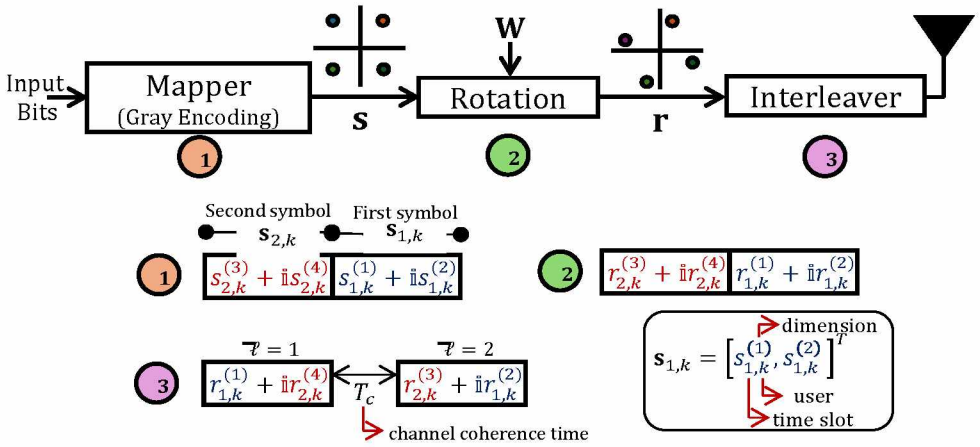

Figure 3.2: Transmitter and receiver structure with SSD applied to the RIS-assisted communication system.

It is important to emphasize that the benefits provided by SSD depend on the amount of spatial diversity already offered by the RIS. When the number of RIS elements is relatively small, the overall system diversity is limited, and SSD can provide noticeable additional gains by introducing signal-domain diversity that mitigates deep fading events. In these scenarios, SSD effectively complements the RIS by enhancing robustness without requiring additional hardware resources.

On the other hand, when the RIS comprises a large number of reflecting elements, the system already benefits from a high spatial diversity order. In such cases, the incremental gain introduced by SSD becomes more marginal, as the dominant diversity contribution

is governed by the RIS array itself. Nevertheless, even in this regime, SSD can still offer moderate performance improvements, particularly in severe fading conditions or when operating at high modulation orders, at the cost of increased computational complexity only.

For the sake of clarity and without loss of generality, the subsequent analysis considers a two-dimensional SSD configuration as a representative case. The input to the mapper is a sequence of coded bits. After Gray mapping, every pair of complex symbols is expressed as

$$\mathbf{s}_k = \begin{bmatrix} s_{1,k} \\ s_{2,k} \end{bmatrix}, \tag{3.33}$$

where k denotes the time-slot index.

Each complex symbol is written as

$$s_{1,k} = s_{1,k}^{(I)} + j\, s_{1,k}^{(Q)}, \qquad s_{2,k} = s_{2,k}^{(I)} + j\, s_{2,k}^{(Q)}, \tag{3.34}$$

where (I) and (Q) represent the in-phase and quadrature components, respectively. The superscripts (1) and (2) refer to the first and second symbol in the pair.

The two mapped symbols are rotated through a unitary 2×2 matrix $\mathbf{W}$:

$$\mathbf{r}_k = \mathbf{W}\, \mathbf{s}_k = \begin{bmatrix} r_{1,k} \\ r_{2,k} \end{bmatrix}. \tag{3.35}$$

The rotation matrices were indicated previously in Table 2.2. After the rotation process, the rotated symbols can be represented as

$$r_{1,k} = r_{1,k}^{(I)} + i\, r_{1,k}^{(Q)}, \qquad r_{2,k} = r_{2,k}^{(I)} + i\, r_{2,k}^{(Q)}. \tag{3.36}$$

The interleaver reorders the real and imaginary components of $\mathbf{r}_k$ according to the channel coherence time T_c, i.e., the number of symbols that experience the same channel

realization.

Case 1 (independent channels), no permutation is applied:

$$\tilde{r}_{1,k} = r_{1,k}, \qquad \tilde{r}_{2,k} = r_{2,k}. \tag{3.37}$$

Case 2 (two consecutive symbols share the same channel), to reduce correlation, the interleaver mixes the in-phase and quadrature components:

$$\tilde{r}_{1,k} = r_{1,k}^{(I)} + i\, r_{2,k}^{(Q)}, \qquad \tilde{r}_{2,k} = r_{2,k}^{(I)} + i\, r_{1,k}^{(Q)}. \tag{3.38}$$

At the receiver, deinterleaving and inverse rotation are performed to reconstruct the original symbol vector before demodulation. A minimum-distance detector is employed to identify the transmitted symbol by minimizing the Euclidean distance between the received vector and the possible rotated constellation points. This detection process effectively combines the independent fading effects across dimensions, yielding additional diversity gain.

In the context of the proposed RIS-assisted system under MFTR fading, the inclusion of SSD modifies only the modulation and detection stages, while the RIS-assisted propagation model remains unchanged. This allows a direct comparison between systems with and without SSD to quantify the performance improvement solely attributable to SSD. The impact of SSD is assessed through Monte Carlo simulations of the ABEP under various configurations of RIS elements and constellation rotation parameters.

In summary, the system and performance analyses developed in this chapter establish the mathematical foundation required to characterize RIS-assisted communications under MFTR fading, with and without the incorporation of SSD. The derived expressions for the instantaneous SNR, outage probability, and ABEP provide the analytical tools needed to assess the system behavior under different propagation and configuration scenarios. Having defined the complete theoretical model, the next chapter presents detailed numerical simulations that validate these analytical formulations and illustrate the

practical performance benefits achieved through RIS deployment and SSD integration.

4 NUMERICAL RESULTS AND DISCUSSIONS

In this section, we present numerical results and discuss the OP and ABEP of the considered RIS-assisted wireless system across various representative scenarios. The accuracy of the analytical expressions is corroborated through Monte Carlo simulations, using the software MATLAB with 5×10^8 iterations. The system parameters used in each figure were selected to illustrate representative scenarios and to validate the accuracy of the provided expressions.

Unless otherwise stated, the simulations adopt the following system parameters. The transmitter–RIS link is set to $d_1 = 50$ m with a path-loss exponent of $\alpha_1 = 2.6$, whereas the RIS–receiver link is modeled with $d_2 = 40$ m and a path-loss exponent of $\alpha_2 = 2.8$. For both links, the path-loss factor is $\mathcal{K}_1 = \mathcal{K}_2 = -30$ dB. These values are consistent with the propagation conditions typically encountered in urban and indoor environments at sub-THz frequencies [39, 40].

4.1 Outage Probability

In this subsection, the OP curves for different operating scenarios are presented. These results provide a comparative view of how system performance varies with key parameters such as the number of RIS elements, link distances, transmit power, and fading conditions.

Figs. 4.1, and 4.2 show the OP as a function of the number of RIS elements N, parameterized by different wireless system configurations. In these figures, the label *same channel* indicates that both the transmitter–RIS and RIS–receiver links are modeled with MFTR fading channels with identical parameters: $m = 4$, $K = 5/2$, $\mu = 2$, and $\Delta = 3/5$. On the other hand, the label *different channel* refers to the case in which the transmitter–RIS and RIS–receiver links are subject to MFTR fading channels with different parameter sets. Specifically, the transmitter–RIS link is characterized by the

parameters above, while the RIS–receiver link follows an MFTR distribution with $m = 2$, $K = 5/2$, $\mu = 4$, and $\Delta = 3/5$.

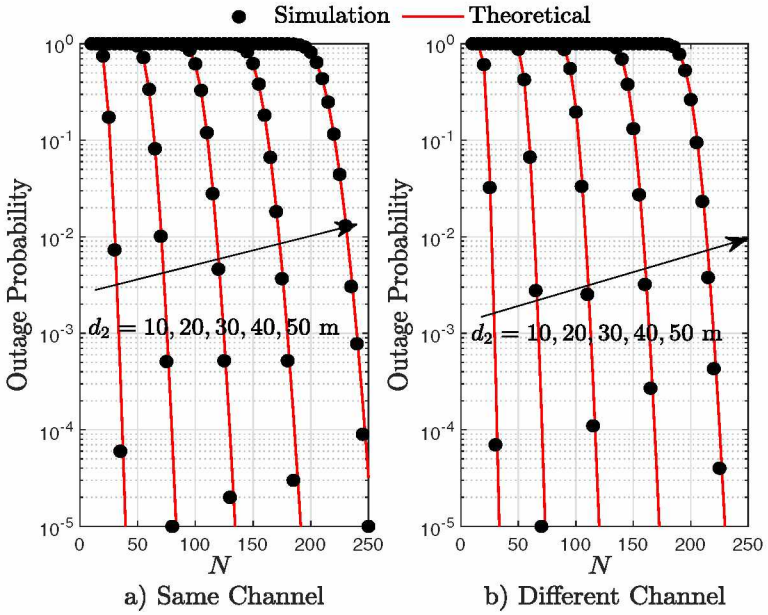

Figure 4.1: OP as function of N, parameterized by the distance d_2.

In particular, Fig. 4.1 shows the OP as a function of N, parameterized by the distance d_2 with $d_1 = 60$ m and $P_t = 19$ dBm. The results indicate that the OP decreases monotonically with N owing to the RIS array gain, where shorter d_2 values naturally yield superior performance. Furthermore, the *different channel* case achieves slightly better performance in the high-N regime. Specifically, in the *same channel* scenario, both links are modeled with MFTR fading with $\mu = 4$. In contrast, in the *different channel* scenario, the transmitter–RIS link is affected by MFTR fading with $\mu = 4$, while the RIS–receiver link experiences MFTR fading with $\mu = 2$.

From the numerical results, it is observed that an increase of μ in the first link implies a larger number of multipath clusters, which corresponds to a richer propagation environment and enhanced channel diversity [24]. Consequently, the *different channel* scenario exhibits a lower outage probability compared to the *same channel* case. From a quantitative perspective, this improvement translates into a modest gain of a few decibels in the required transmit power (or equivalently, a slight reduction in OP for a fixed N), particularly noticeable in the moderate N regime. Nevertheless, this gain remains

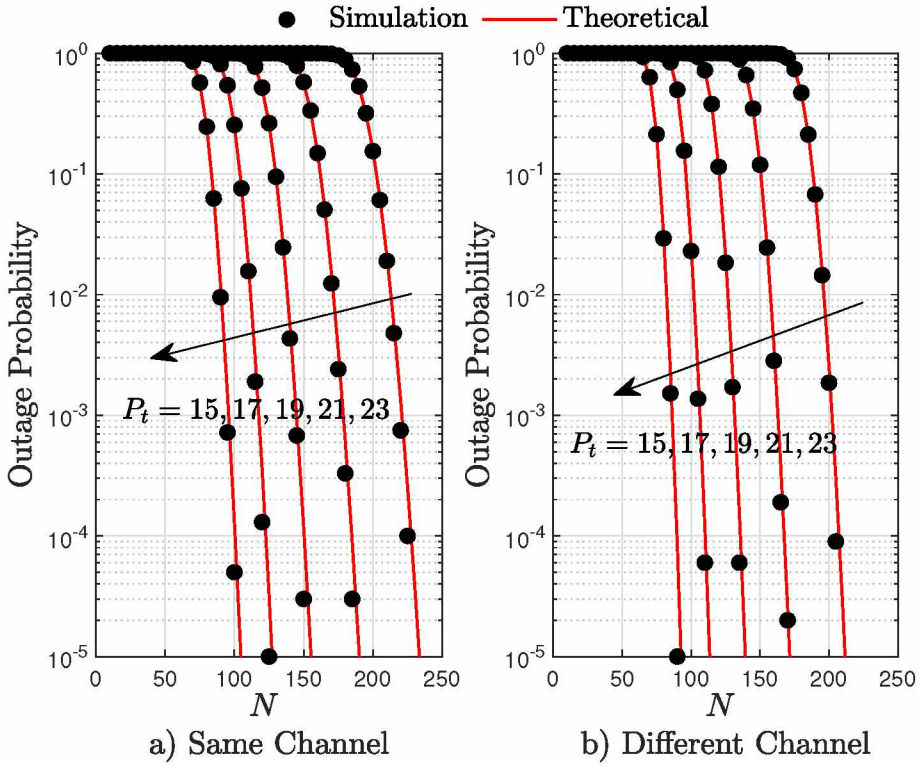

Figure 4.2: OP as function of N, parameterized by P_{t}.

limited, since the overall system diversity is predominantly governed by the large number of RIS elements, which provides a much stronger array and spatial diversity gain than the increase in μ alone.

On the other hand, Fig. 4.2 illustrates the OP as a function of N, parameterized by the transmit power P_t expressed in dBm. As expected, increasing P_t reduces the OP, thereby requiring fewer RIS elements to achieve a target performance level. Similar to Fig. 4.1, the *different channel* scenario yields a slightly lower OP in the high-N region. Finally, an important observation in Figs. 4.1 and 4.2 is the close agreement between the simulation and analytical results, which validates the derived expressions and highlights the dependence of the system performance on the different system and channel parameters.

As reported in [22, Table I], the MFTR model can emulate a wide range of fading channels by adjusting the distribution parameters m, K, μ, and Δ. Building on this property, the numerical analysis is further extended to assess a range of scenarios associated with different fading models. Accordingly, Fig. 4.3 illustrates the OP as a function of N,

with each curve representing a distinct MFTR parameter configuration under the condition $P_t = 19$ dBm. The parameter sets adopted for each fading model are summarized in Table 4.1, and are consistent with those in [22, Table I]. The same parameter settings are applied to both the transmitter–RIS and RIS–receiver links.

Table 4.1: MFTR channel parameters for different fading models.

Fading model	**m**	**K**	$\boldsymbol{\mu}$	$\boldsymbol{\Delta}$
Rayleigh	5	0	1	0
Rician	50	2.5	1	0
κ-μ shadowed	2	4	2	0
FTR	2	2.5	1	0.6

The results presented in Fig. 4.3 clearly indicate that Rayleigh fading necessitates the largest number of RIS elements to achieve the target outage probability (OP), thereby confirming its characterization as the most adverse propagation condition, attributable to the absence of a line-of-sight (NLoS) component. In contrast, the Rician and FTR scenarios exhibit a faster decay in the OP as N increases, due to the presence of dominant specular components in their channel structure. The κ-μ shadowed model exhibits the best performance among the considered cases because its parameter configuration corresponds to a richer multipath environment with enhanced diversity. Overall, these results highlight how the flexibility of the MFTR model and our derived expressions allow the evaluation of RIS-assisted systems under a broad range of fading conditions, from severe NLoS propagation to scenarios with strong multipath clustering and specular dominance.

4.2 Average Bit Error Probability

In this subsection, we present numerical results for the ABEP obtained under different operating conditions. M-QAM modulation is adopted to parameterize the system across diverse scenarios. For simulation purposes, the noise power is set to -123.2 dBm, which corresponds to the thermal noise floor at room temperature (290 K) with an effective bandwidth of approximately 120 kHz, as defined in [41]. This subcarrier spacing, specified for mmWave and FR2 operation in the 5G NR architecture, is particularly suit-

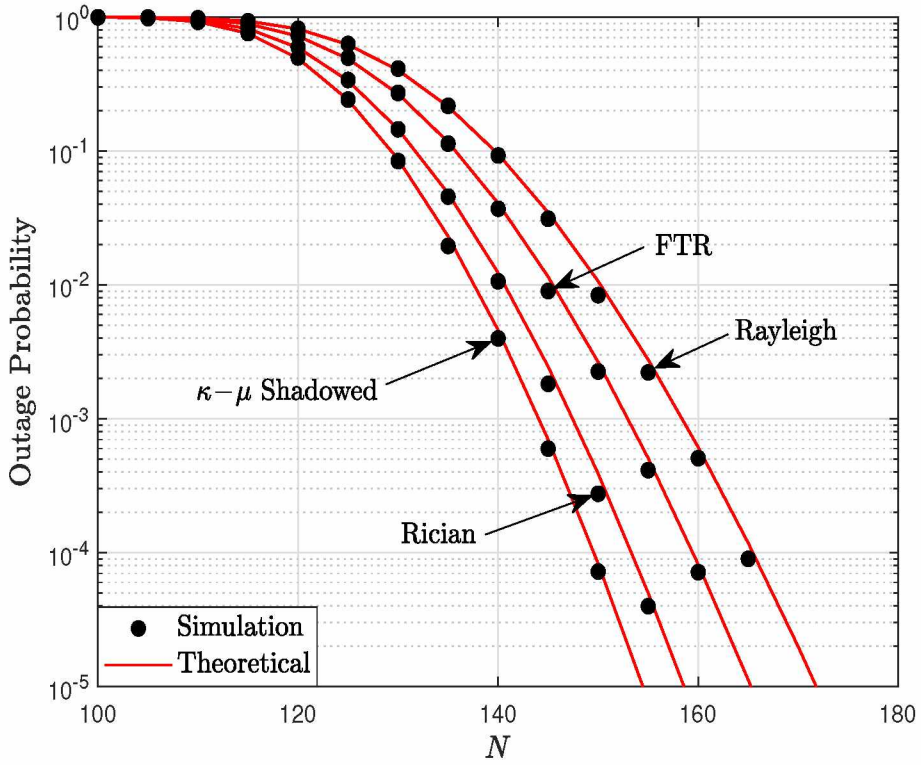

Figure 4.3: OP as function of N, parameterized by the different fading channel scenarios indicated in Table 4.1.

able for high-frequency systems, as it mitigates Doppler effects and allows for shorter symbol durations.

In the following figures, the exact *theoretical* ABEP is obtained through numerical evaluation of the integral in (3.27), while the *approximate* ABEP is computed using the closed-form expression given in (3.32).

Fig. 4.4 illustrates the ABEP as a function of the transmission power P_t, parameterized by the modulation order M, for a RIS-assisted system operating under MFTR fading. The simulation setup assumes a transmitter-RIS distance $d_1 = 70$ m and a RIS-receiver distance $d_2 = 40$ m, with both links subject to a path-loss factors of $\mathcal{K}_1 = \mathcal{K}_2 = -30$ dB and a path-loss exponents $\alpha_1 = \alpha_2 = 3$. The RIS comprises $N = 200$ reflecting elements. The fading channels are modeled according to the MFTR distribution with parameters $m_1 = 4, \mu_1 = 2, K_1 = 5/2, \Delta_1 = 3/5$ for the transmitter-RIS link and $m_2 = 2, \mu_2 = 4, K_2 = 5/2, \Delta_2 = 3/5$ for the RIS-receiver link. As expected, increasing M leads to a higher ABEP, while increasing P_t reduces the ABEP. More importantly, the

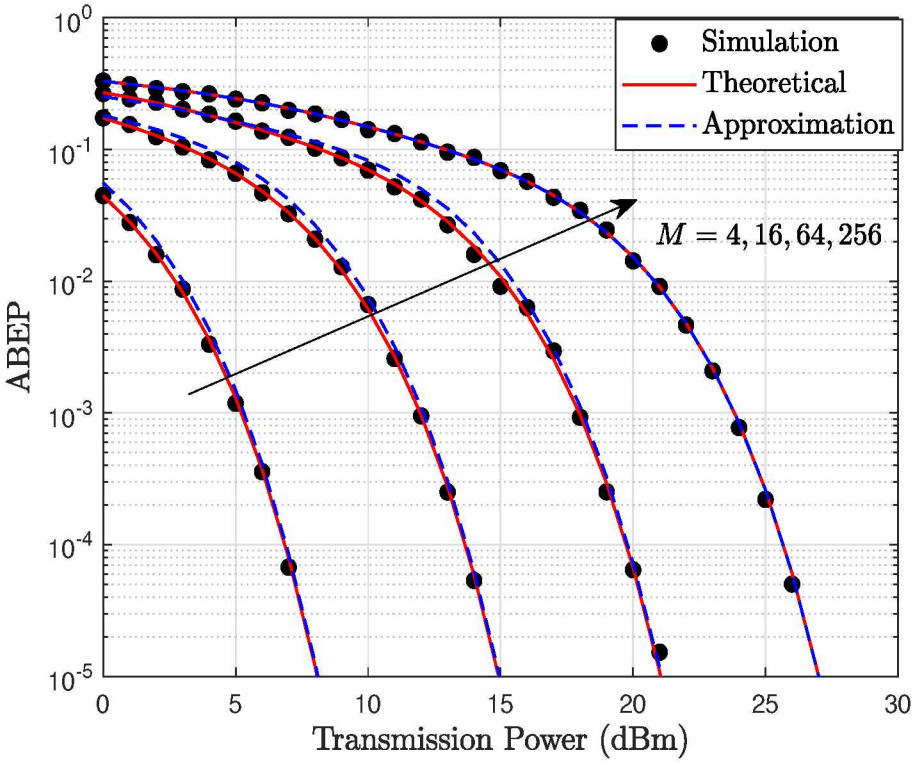

Figure 4.4: ABEP as a function of P_t, parameterized by the modulation order M.

results demonstrate excellent agreement between the simulation curves and the analytical expression in (3.32), even for high modulation orders such as 256-QAM, which confirms the precision of the proposed derivation.

Fig. 4.5 uses the same fading channel parameters as Fig. 4.4; however, it highlights the beneficial effect of increasing the number of RIS elements in this case. These results are based on 256-QAM modulation. As N increases, the system requires substantially less transmit power to achieve a given target ABEP, and the error probability decreases at a significantly faster rate. This trend demonstrates the array gain provided by the RIS, which directly enhances the link reliability and robustness. Furthermore, the results reveal an excellent agreement between the simulation, theoretical, and approximate curves, confirming the accuracy of the proposed analytical framework. Overall, these findings highlight the strong potential of RIS-assisted communications, where even moderate increases in N can substantially improve energy efficiency and quality of service even for high-order modulations like 256-QAM.

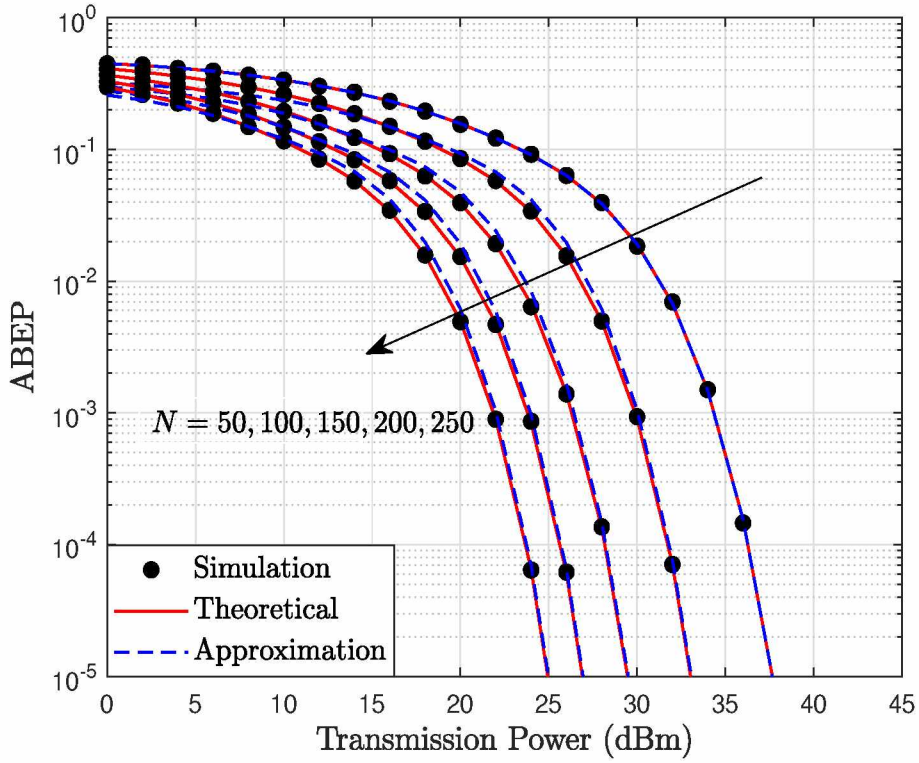

Figure 4.5: ABEP as a function of P_t, parameterized by the number of RIS elements N, and considering 256-QAM.

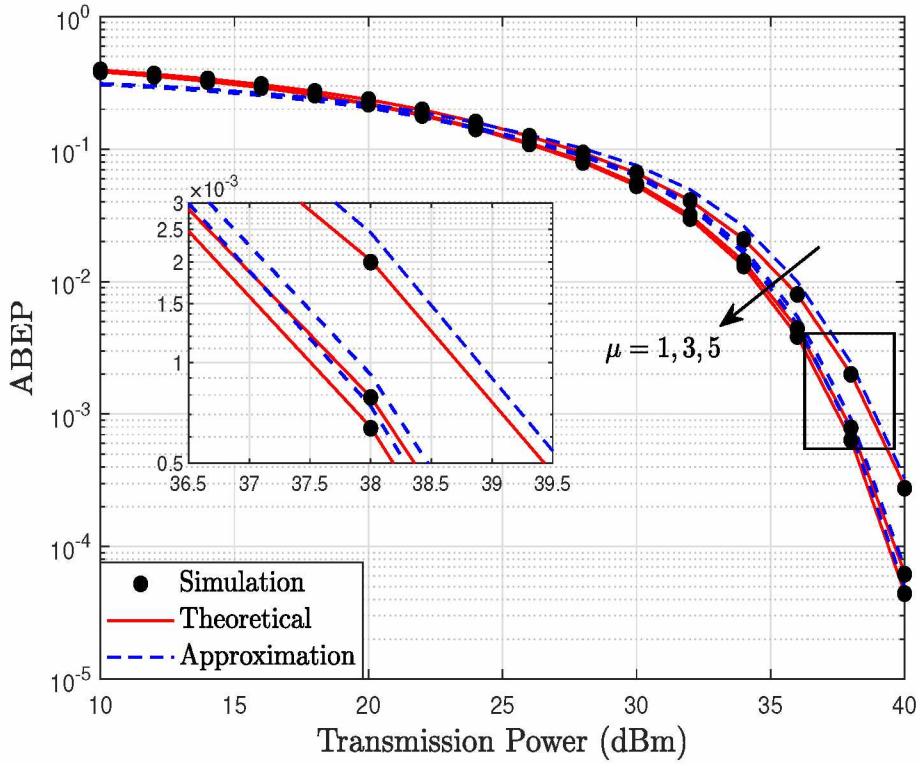

Figure 4.6: ABEP as function of P_t, parameterized by different values for μ, and considering 256-QAM.

Fig. 4.6 shows the ABEP performance of a RIS-assisted system under MFTR fading, parameterized by the number of multipath clusters $\mu = \{1,3,5\}$ in both links. The scenario considers 256-QAM, $d_1 = 70$ m and $d_2 = 40$ m with path-loss factors of $\mathcal{K}_1 = \mathcal{K}_2 = -30$ dB and a path-loss exponent $\alpha_1 = \alpha_2 = 3$. The RIS employs $N = 40$ elements. Both links follow the MFTR fading model with $m_1 = m_2 = 2$, $K_1 = K_2 = 5/2$, $\Delta_1 = \Delta_2 = 3/5$. The results indicate that as μ increases, the system performance improves because a higher number of multipath clusters enhances channel diversity. However, this improvement is relatively modest compared to the substantial diversity already provided by the large number of RIS elements. These results highlight that even in scenarios with unfavorable propagation conditions, RIS can significantly enhance system performance, maintaining low ABEP levels even for high modulation orders such as 256-QAM.

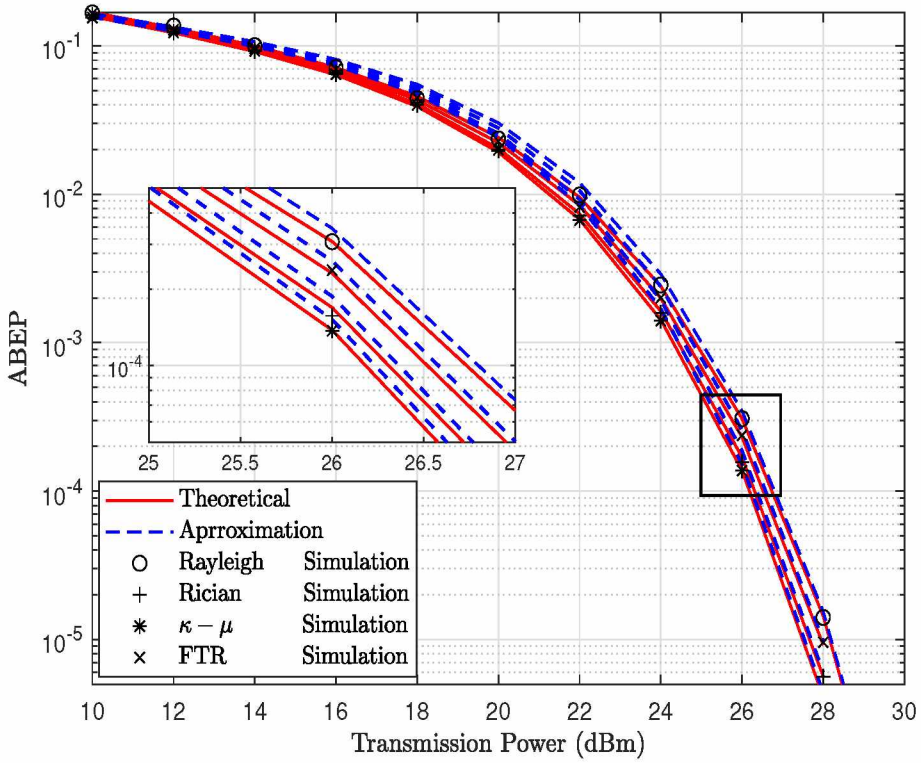

Figure 4.7: ABEP as function of P_t, parameterized by the different fading channel scenarios indicated in Table 4.1, considering $N = 200$ and $M = 256$.

Fig. 4.7 illustrates the ABEP as a function of the transmit power for four representative fading models Rayleigh, Rician, κ–μ, and FTR whose corresponding parameters are listed in Table 4.1. The results show an excellent agreement between the simulation, the-

oretical, and approximate curves, validating the accuracy and reliability of the proposed analytical framework. From a comparative perspective, the Rayleigh model exhibits the poorest performance, yielding the highest ABEP for a given transmit power. The Rician channel provides noticeable improvement, while the κ–μ and FTR models achieve lower error probabilities. The slopes of the curves in the high power region reveal the inherent diversity gains of each fading model: Rayleigh fading exhibits the lowest diversity, whereas the κ–μ and FTR channels display steeper decays, reflecting more favorable propagation conditions. However, the difference in diversity gain across the models remains relatively small, since the large number of RIS elements inherently provides high spatial diversity, thereby mitigating the effect of fading variations between channels. A zoomed-in view is provided in the figure to highlight these effects more clearly. Overall, the results confirm both the analytical soundness of the proposed model and the practical relevance of advanced fading characterizations.

4.3 Simulation-Based Evaluation of SSD in RIS-Assisted Systems under MFTR Fading

To evaluate the impact of incorporating SSD into RIS-assisted systems operating under MFTR fading, a series of simulation experiments were carried out using the baseline RIS–MFTR framework described previously. SSD was integrated at both the transmitter and receiver by applying a two-dimensional rotation to the M-QAM constellation. As this constitutes the first attempt to combine SSD with RIS-assisted communications in an MFTR environment, the analysis focuses on two-dimensional rotations, although the framework naturally extends to higher dimensions.

The system parameters were aligned with the analytical MFTR-based model, using $m = 20$, $\mu = 1$, $K = 0.1$, and $\Delta = 0.5$, which represent moderate specular fluctuation and a single dominant multipath cluster. Path-loss exponents were set to $\alpha_1 = 2.6$ with $k_1 = k_2 = -30\,\text{dB}$, and the distances between the nodes were defined as $d_1 = 30\,\text{m}$ (Tx–RIS) and $d_2 = 20\,\text{m}$ (RIS–Rx).

Fig. 4.8 shows the ABEP of the aforementioned system as a function of the rotation parameter λ_2. This figure illustrates that different values of λ_2 lead to distinct ABEP levels. The search for the optimal value of this parameter can be carried out in several ways—for example, through an exhaustive brute–force search aimed at minimizing a specific performance metric such as the ABEP, or through more sophisticated mathematical optimization techniques. The most appropriate approach will depend on the underlying fading–channel parameters as well as the particular system configuration. Nevertheless, this optimization analysis lies beyond the scope of the present work and is therefore left as an option for future research.

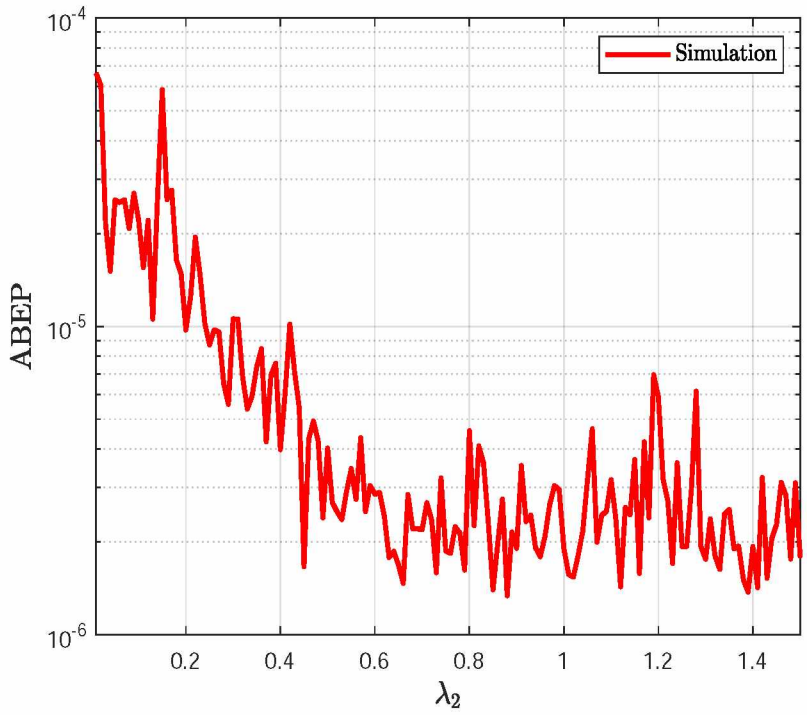

Figure 4.8: Simulated ABEP of the RIS-assisted system under MFTR fading as a function of the rotation parameter λ_2.

By considering the previous results, the SSD rotation factor was fixed to $\lambda_2 = 0.6$ in order to clearly highlight the impact of constellation rotation on the analyzed RIS-assisted system.

Accordingly, Fig. 4.9 illustrates the ABEP of the RIS–SSD system as a function of the transmit power. The results show that SSD provides consistent performance improve-

ments across all evaluated RIS configurations. For example, at an ABEP level of 10^{-5} with $N = 10$ elements, SSD offers an approximate transmit-power gain of about 2.5 dB. Although this gain is moderate, it is non-negligible and becomes particularly relevant under the severe conditions imposed by the MFTR fading model. Furthermore, the relative benefit of SSD is more evident for smaller values of N, which is consistent with the fact that SSD guarantees a fixed diversity order of $\mathcal{D} = 2$, whereas the inherent spatial diversity provided by the RIS increases with N. Hence, SSD plays a more prominent role when the available spatial diversity is limited.

It is worth noting that the reported ABEP values could be further improved, as $\lambda_2 = 0.6$ is not necessarily the globally optimal rotation parameter under the considered operating conditions.

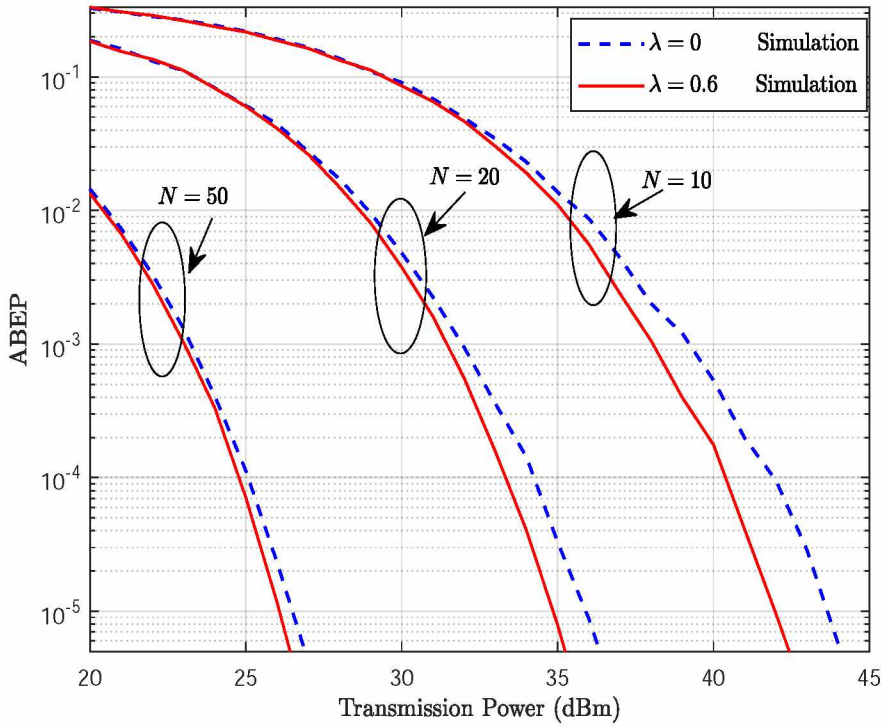

Figure 4.9: Simulated ABEP performance of the RIS-assisted system under MFTR fading with and without SSD for different numbers of RIS elements N.

Reaching even lower ABEP regions would reveal larger relative improvements; however, such regions require extensive Monte Carlo simulations, which become computationally prohibitive. Despite this, SSD remains attractive because it enhances link reliability

without requiring additional RIS elements, RF chains, or hardware complexity—only an increase in computational processing.

Beyond performance gains, SSD potentially enhances physical-layer security, as the rotation parameter λ_2 may be treated as a cryptographic key shared exclusively between transmitter and receiver. This promising direction is left open for future research.

5 FINAL CONSIDERATIONS

5.1 Principal Conclusions

This work has addressed, for the first time, the performance analysis of RIS-assisted communication systems operating over MFTR fading channels, a scenario that, to the best of our knowledge, had not been previously investigated in the literature. Unlike conventional fading models, the MFTR framework enables a unified representation of diverse propagation conditions, offering greater flexibility for system-level analysis. An additional advantage of the proposed formulations is that the resulting expressions are simple to evaluate using standard mathematical software, which facilitates their application to a wide range of scenarios. This is particularly relevant since the MFTR model generalizes many classical fading distributions as special cases, including Nakagami-m, Rician, Rician shadowed, κ–μ, κ–μ shadowed, η–μ, two-wave, TWDP, and FTR.

Closed-form approximate expressions for both the outage probability (OP) and the average bit error probability (ABEP), under M-QAM modulation, were derived and validated across a wide range of scenarios. It is important to indicate that the proposed analytical results rely on the Central Limit Theorem, whose accuracy improves as the number of RIS elements increases. Consequently, the analytical framework is particularly suitable for RIS deployments with a moderate-to-large number of reflecting elements, which correspond to the most relevant practical operating regimes.

A comprehensive evaluation of key system parameters including fading channel characteristics, transmit power, and the number of RIS elements was carried out. The results indicate that increasing the number of RIS elements N provides the most significant and consistent performance improvement, as it directly enhances spatial diversity and array gain. Improvements in the propagation environment, reflected by larger values of the MFTR parameter μ, also lead to performance gains; however, these gains are generally

less pronounced than those obtained by increasing N, especially when the RIS is already large.

In addition, a simulation-based study was performed to investigate the integration of Signal Space Diversity (SSD) into the RIS-assisted system under MFTR fading. The results demonstrated that SSD improves link reliability by enhancing diversity in the signal domain without requiring additional RF hardware. From a system design perspective, SSD is particularly beneficial when the number of RIS elements is limited or when the channel conditions are severe, where spatial diversity alone may be insufficient. When a large number of RIS elements is available, the additional gains provided by SSD become more modest, yet remain non-negligible in high-reliability operating regions.

Based on these observations, a practical design guideline can be drawn: increasing the number of RIS elements should be the primary strategy to improve system performance, followed by improvements in the propagation environment when feasible, while SSD constitutes an attractive complementary technique that enhances robustness at low computational cost and without additional hardware complexity.

A rigorous analytical characterization of RIS–SSD systems under MFTR fading, optimized rotation design tailored to channel statistics, and extended investigations in ultra-low ABEP regimes and physical-layer security applications remain promising directions for future research.

5.2 Future Work

Future research directions can extend the current study in several ways. First, the analytical framework could be generalized to account for independent but non-identically distributed (i.n.i.d.) fading channels, as well as spatial correlation among the RIS elements or between the transmitter–RIS and RIS–receiver links. Such extensions would provide a more realistic modeling of practical RIS deployments.

Second, incorporating practical system impairments such as channel estimation errors, quantized phase control, synchronization imperfections, and hardware non-linearities

would allow the proposed model to more accurately capture the behavior of real-world RIS systems.

Another promising avenue involves developing closed-form approximations or bounding techniques for the joint RIS–SSD–MFTR configuration, as the current study relied exclusively on simulations. Analytical characterization of this combined scenario remains an open and challenging problem.

Finally, future works may explore the integration of machine learning-based RIS optimization and adaptive SSD parameter tuning, allowing dynamic adjustment of reflection coefficients and constellation rotation based on instantaneous channel conditions. Such hybrid approaches could further enhance system adaptability, spectral efficiency, and energy performance in next-generation wireless networks.

BIBLIOGRAPHY

[1] A. Goldsmith, *Wireless Communications*. Cambridge, UK: Cambridge University Press, 2005.

[2] H. Carvajal, *Bit Error Rate and Spectral Efficiency Evaluation of MC-CDMA Cellular Systems Employing Multiuser Detection*. PhD thesis, Universidade Estadual de Campinas (UNICAMP), Apr. 2018.

[3] J. Kaur and M. A. Khan, "Sixth generation (6g) wireless technology: An overview, vision, challenges and use cases," in *2022 IEEE Region 10 Symposium (TENSYMP)*, pp. 1–6, 2022.

[4] J. Huang, C.-X. Wang, Y. Sun, R. Feng, J. Huang, B. Guo, Z. Zhong, and T. J. Cui, "Reconfigurable intelligent surfaces: Channel characterization and modeling," *Proceedings of the IEEE*, vol. 110, no. 9, pp. 1290–1311, 2022.

[5] Q. Wu, S. Zhang, B. Zheng, C. You, and R. Zhang, "Intelligent reflecting surface-aided wireless communications: A tutorial," *IEEE Transactions on Communications*, vol. 69, no. 5, pp. 3313–3351, 2021.

[6] E. G. Gomes, H. R. C. Mora, and E. E. B. Olivo, "Performance of star-ris-aided rsma networks: Impact of correlated fading channels and sic imperfections," *IEEE Access*, vol. 13, pp. 39826–39839, 2025.

[7] C. D. Altamirano, J. Minango, H. C. Mora, and C. De Almeida, "Ber evaluation of linear detectors in massive mimo systems under imperfect channel estimation effects," *IEEE Access*, vol. 7, pp. 174482–174494, 2019.

[8] E. Björnson, O. Özdogan, and E. G. Larsson, "Intelligent reflecting surface versus decode-and-forward: How large surfaces are needed to beat relaying?," *IEEE Wireless Communications Letters*, vol. 9, no. 2, pp. 244–248, 2020.

[9] I. Yetenek, C. Edemen, M. Elamassie, and M. Uysa, "Comparative study of reconfigurable intelligent surfaces against relay systems: Amplify-and-forward and decode-and-forward approaches," in *2024 IEEE International Black Sea Conference on Communications and Networking (BlackSeaCom)*, pp. 300–303, 2024.

[10] M. Di Renzo, K. Ntontin, J. Song, F. H. Danufane, X. Qian, F. Lazarakis, J. De Rosny, D.-T. Phan-Huy, O. Simeone, R. Zhang, M. Debbah, G. Lerosey, M. Fink, S. Tretyakov, and S. Shamai, "Reconfigurable intelligent surfaces vs. relaying: Differences, similarities, and performance comparison," *IEEE Open Journal of the Communications Society*, vol. 1, pp. 798–807, 2020.

[11] D. Shahbaztabar, I. Trigui, W.-P. Zhu, and W. Ajib, "Performance analysis of ris-assisted communication with direct link: A new copula application," *IEEE Open Journal of the Communications Society*, vol. 5, pp. 1740–1752, 2024.

[12] M. Mukherjee, V. Kumar, M. Guo, D. B. da Costa, E. Basar, and Z. Ding, "The interplay of reconfigurable intelligent surfaces and mobile edge computing in future wireless networks: A win-win strategy to 6g," *ArXiv*, vol. abs/2106.11784, 2021.

[13] W. Tang, M. Z. Chen, X. Chen, J. Y. Dai, Y. Han, M. Di Renzo, Y. Zeng, S. Jin, Q. Cheng, and T. J. Cui, "Wireless communications with reconfigurable intelligent surface: Path loss modeling and experimental measurement," *IEEE Transactions on Wireless Communications*, vol. 20, no. 1, pp. 421–439, 2021.

[14] B. V. Mone, H. H. Nuha, H. R. Putra Sailellah, and A. H. Basri, "Rayleigh fading modeling for reconfigurable intelligent surfaces under different number of elements," in *2024 International Conference on Decision Aid Sciences and Applications (DASA)*, pp. 1–5, 2024.

[15] U. Mutlu, M. Bilim, and Y. Kabalci, "Outage probability analysis of ris-assisted system over weibull/rayleigh fading channels," in *2024 6th Global Power, Energy and Communication Conference (GPECOM)*, pp. 699–703, 2024.

[16] M. Li, K. Xue, W. Chen, and Z. Han, "Secure performance of ris-aided noma in cognitive v2x networks with imperfect csi over double rayleigh fading," *IEEE Transactions on Cognitive Communications and Networking*, vol. 10, no. 4, pp. 1339–1355, 2024.

[17] A. Al-Rimawi and A. Al-Dweik, "On the performance of ris-assisted communications with direct link over κ-μ shadowed fading," *IEEE Open Journal of the Communications Society*, vol. 3, pp. 2314–2328, 2022.

[18] H. Du, J. Zhang, J. Cheng, and B. Ai, "Millimeter wave communications with reconfigurable intelligent surfaces: Performance analysis and optimization," *IEEE Transactions on Communications*, vol. 69, no. 4, pp. 2752–2768, 2021.

[19] C. R. N. da Silva, N. Simmons, M. C. L. Alvarado, P. C. Sofotasios, S. L. Cotton, and M. D. Yacoub, "α-μ, κ-μ, and η-μ mixed products: Exact and simple-approximate solutions, and practical and ris applications," *IEEE Transactions on Vehicular Technology*, vol. 73, no. 10, pp. 14734–14748, 2024.

[20] P. V. Trinh and S. Sugiura, "Maximum secrecy throughput analysis of practical ris-aided mmwave systems over unified ftr/iftr fading channels," *IEEE Transactions on Wireless Communications*, vol. 23, no. 11, pp. 16590–16605, 2024.

[21] E. Basar, M. Di Renzo, J. De Rosny, M. Debbah, M.-S. Alouini, and R. Zhang, "Wireless communications through reconfigurable intelligent surfaces," *IEEE Access*, vol. 7, pp. 116753–116773, 2019.

[22] J. D. V. Sánchez, F. J. Lopez-Martinez, J. F. Paris, and J. M. Romero-Jerez, "The multi-cluster fluctuating two-ray fading model," *IEEE Transactions on Wireless Communications*, vol. 23, no. 5, pp. 4199–4213, 2024.

[23] J. F. Paris, "Statistical characterization of κ–μ shadowed fading," *IEEE Transactions on Vehicular Technology*, vol. 63, no. 2, pp. 518–526, 2014.

[24] N. O. Garzón, H. C. Mora, F. A. García, J. Vega-Sánchez, and D. M. Osorio, "Performance evaluation of mrc systems over sub-terahertz mftr fading channels," *IEEE Communications Letters*, vol. 28, no. 10, pp. 2422–2426, 2024.

[25] A. Sikri, A. Mathur, and G. Kaddoum, "Signal space diversity-based distributed ris-aided dual-hop mixed rf-fso systems," *IEEE Communications Letters*, vol. 26, no. 5, pp. 1066–1070, 2022.

[26] B. Sklar, *Digital Communications: Fundamentals and Applications*. Upper Saddle River, NJ, USA: Prentice Hall, 2 ed., 2001.

[27] C. E. Shannon, "A mathematical theory of communication," *Bell System Technical Journal*, vol. 27, no. 3, pp. 379–423, 1948.

[28] M. D. Yacoub, "The α–μ distribution: A physical fading model for the stacy distribution," *IEEE Transactions on Vehicular Technology*, vol. 56, no. 1, pp. 27–34, 2007.

[29] M. Abramowitz and I. A. Stegun, *Handbook of Mathematical Functions with Formulas, Graphs, and Mathematical Tables*. Washington, DC: US Dept. of Commerce: National Bureau of Standards, 10 ed., 1972.

[30] M. Di Renzo, A. Zappone, M. Debbah, M.-S. Alouini, C. Yuen, J. de Rosny, and S. Tretyakov, "Smart radio environments empowered by reconfigurable intelligent surfaces: How it works, state of research, and road ahead," *IEEE Journal on Selected Areas in Communications*, vol. 38, no. 11, pp. 2450–2525, 2020.

[31] Q. Wu and R. Zhang, "Intelligent reflecting surface enhanced wireless network via joint active and passive beamforming," *IEEE Transactions on Wireless Communications*, vol. 18, no. 11, pp. 5394–5409, 2019.

[32] E. Başar and et al., "Reconfigurable intelligent surfaces for 6g wireless networks: A communication-theoretic perspective," *IEEE Wireless Communications*, vol. 27, no. 6, pp. 118–124, 2020.

[33] J. Boutros and E. Viterbo, "Signal space diversity: A power- and bandwidth-efficient diversity technique for the rayleigh fading channel," *IEEE Transactions on Information Theory*, vol. 44, pp. 1453–1467, 07 1998.

[34] E. Basar, M. Di Renzo, J. De Rosny, M. Debbah, M.-S. Alouini, and R. Zhang, "Wireless communications through reconfigurable intelligent surfaces," *IEEE Access*, vol. 7, pp. 116753–116773, 2019.

[35] W. Tang, X. Chen, M. Z. Chen, J. Y. Dai, Y. Han, S. Jin, Q. Cheng, G. Y. Li, and T. J. Cui, "On channel reciprocity in reconfigurable intelligent surface assisted wireless networks," *IEEE Wireless Communications*, vol. 28, no. 6, pp. 94–101, 2021.

[36] A. Papoulis, *Probability, Random Variables, and Stochastic Processes.* New York: McGraw-Hill, 4 ed., 2002.

[37] K. Cho and D. Yoon, "On the general BER expression of one- and two-dimensional amplitude modulations," *IEEE Trans. Commun.*, vol. 50, no. 7, pp. 1074–1080, 2002.

[38] M. Chiani, D. Dardari, and M. K. Simon, "New exponential bounds and approximations for the computation of error probability in fading channels," *IEEE Transactions on Wireless Communications*, vol. 2, pp. 840–845, 7 2003.

[39] "Ieee standard for high data rate wireless multi-media networks—amendment 2: 100 gb/s wireless switched point-to-point physical layer," 2017.

[40] S. Priebe, M. Jacob, and T. Kürner, "Angular and polarization characteristics of scattering at 60 ghz in indoor environments," *IEEE Transactions on Antennas and Propagation*, vol. 61, no. 1, pp. 292–301, 2013.

[41] 3rd Generation Partnership Project (3GPP), "Technical Specification Group Radio Access Network; NR; Physical Channels and Modulation (Release 15)," Tech. Rep. TS 38.211, v15.2.0, 3GPP, 2018. Available: https://www.3gpp.org/ftp/Specs/archive/38_series/38.211/38211-f20.zip.